Reconciling Mars InSight Results, Geoid, and Melt Evolution with 3D Spherical Models of Convection

Josh P. Murphy[1] and Scott D. King[1]

[1]Virginia Tech

December 14, 2023

Abstract

We investigate the geodynamic and melting history of Mars using 3D spherical shell models of mantle convection, constrained by the recent InSight mission results. The Martian mantle must have produced sufficient melt to emplace the Tharsis rise by the end of the Noachian–requiring on the order of 1–3×109 km3 of melt after accounting for limited (˜10\%) melt extraction. Thereafter, melting declined, but abundant evidence for limited geologically recent volcanism necessitates some melt even in the cool present-day mantle inferred from InSight data. We test models with two mantle activation energies, and a range of crustal Heat Producing Element (HPE) enrichment factors and initial core-mantle boundary temperatures. We also test the effect of including a hemispheric (spherical harmonic degree-1) step in lithospheric thickness to model the Martian dichotomy. We find that a higher activation energy (350 kJ mol-1) rheology produces present-day geotherms consistent with InSight results, and of those the cases with HPE enrichment factors of 5–10x produce localized melting near or up to present-day. 10x crustal enrichment is consistent with both InSight and geochemical results, and those models also produce present-day geoid power spectra consistent with Mars. However, it is very difficult to produce sufficient melt to form Tharsis in a mantle that also matches the present-day geotherm, without assuming extremely efficient extraction of melt to the surface. The addition of a degree-1 hemispheric dichotomy, as an equatorial step in lithospheric thickness, does not significantly improve upon melt production or the geoid.

Reconciling Mars InSight Results, Geoid, and Melt Evolution with 3D Spherical Models of Convection

J. P. Murphy[1], S. D. King[1]

[1]Virginia Polytechnic Institute and State University
[1]Blacksburg, VA, USA

Key Points:

- Our results favor a higher activation energy mantle rheology and 10x crustal heat producing element enrichment factor
- It is not difficult to produce melt up to the present-day, even with a cool mantle consistent with InSight results
- It is very difficult to produce sufficient melt for Tharsis without assuming extremely efficient extraction of mantle melt to the surface

Corresponding author: Josh Murphy, `jmurph16@vt.edu`

Abstract

We investigate the geodynamic and melting history of Mars using 3D spherical shell models of mantle convection, constrained by the recent InSight mission results. The Martian mantle must have produced sufficient melt to emplace the Tharsis rise by the end of the Noachian–requiring on the order of 1–$3\times10^9\,\mathrm{km}^3$ of melt after accounting for limited ($\sim$10%) melt extraction. Thereafter, melting declined, but abundant evidence for limited geologically recent volcanism necessitates some melt even in the cool present-day mantle inferred from InSight data. We test models with two mantle activation energies, and a range of crustal Heat Producing Element (HPE) enrichment factors and initial core-mantle boundary temperatures. We also test the effect of including a hemispheric (spherical harmonic degree-1) step in lithospheric thickness to model the Martian dichotomy. We find that a higher activation energy ($350\,\mathrm{kJ\,mol^{-1}}$) rheology produces present-day geotherms consistent with InSight results, and of those the cases with HPE enrichment factors of 5–10x produce localized melting near or up to present-day. 10x crustal enrichment is consistent with both InSight and geochemical results, and those models also produce present-day geoid power spectra consistent with Mars. However, it is very difficult to produce sufficient melt to form Tharsis in a mantle that also matches the present-day geotherm, without assuming extremely efficient extraction of melt to the surface. The addition of a degree-1 hemispheric dichotomy, as an equatorial step in lithospheric thickness, does not significantly improve upon melt production or the geoid.

Plain Language Summary

Mars' mantle needed to produce an extremely high volume of melt by $\sim$3.7 billion years ago in order to build the immense volcanic plateau of Tharsis. There is also significant evidence for small volumes of geologically recent volcanism, yet InSight mission results indicate relatively cool mantle at present. We use 3D numerical models of the Martian mantle to determine what properties can produce a melting history and present interior temperatures consistent with InSight results and Mars' volcanic history. We test sets of models with two different mantle activation energies (how sensitive the mantle viscosity is to changes in temperature), and a range of crustal Heat Producing Element enrichment factors. We also test the effect of including a simplified version of the Martian hemispheric dichotomy. Our models with the higher activation energy and 10x crustal enrichment (consistent with Mars' crustal composition) produce melt near the present-day as well as temperature profiles consistent with InSight. However, it is very difficult to produce sufficient melt to form Tharsis in such a cool mantle, without assuming most of the melt produced in the mantle reaches the surface. Addition the simplified dichotomy does not significantly improve our results.

1 Introduction

Results from the InSight mission provide new constraints on the temperature, structure, and geodynamic evolution of the Martian interior. The InSight mission was the first to record quakes (unambiguously) and impacts on Mars (Banerdt et al., 2020; Giardini et al., 2020). Using reflections of seismic waves from the core-mantle boundary of Mars together with geodetic data, Stähler et al. (2021) constrained the radius of the liquid metal core to be 1830±40 km with a mean core density of 5700–6300 kg/m^3–implying that there is 10–15 wt. % S in addition to other light elements dissolved in the nickle-iron core. The core radius is at the large end of the pre-mission estimate (Smrekar et al., 2019) and, implies that there is no bridgmanite layer above the core-mantle boundary. The absence of a bridgmanite layer is an important constraint for mantle dynamics because a thin bridgmanite layer is one mechanism to generate degree-1 convection (Harer & Christensen, 1996; Harder, 1998, 2000).

The topography and crustal thickness of Mars are characterized by the dichotomy between the northern and southern hemispheres. The northern hemisphere is dominated by lowlands which tend to have thinner crust, while the southern hemisphere is dominated by heavily cratered highlands which tend to have a thicker crust. Using InSight seismic data, Knapmeyer-Endrun et al. (2021) found two possible Moho depths, the first at 20±5 km and the second at 39±8 km. The thicker crust is more consistent with the surface composition, while the thinner crust would require an increasing HPE concentration with depth. The thicker crust would also allow a slightly higher bulk crustal density ($3100\,\mathrm{kg\,m^{-3}}$) when compared with the thinner crust ($<2900\,\mathrm{kg\,m^{-3}}$). Considering either model and the aforementioned gravity and topography data sets, Wieczorek et al. (2022) constrain the global average Martian crustal thickness to be between 24 and 72 km, with thinner crust in the lowlands (including the InSight landing site), and thicker crust beneath the highlands and Tharsis.

Huang et al. (2022) constrained the depth of a mid-mantle discontinuity to be 1,006±40 km by modeling triplicated P and S waveforms. Interpreting this seismic discontinuity as the transformation of olivine to a higher-pressure polymorph (likely ringwoodite) yields a mantle potential temperature of 1,605±100 K. Using a parameterized convection approach, Huang et al. (2022) suggest that the mantle potential temperature was 1,720 to 1,860 K soon after formation. When combining the 1,000-depth phase transition transition with an estimated crustal thickness from Knapmeyer-Endrun et al. (2021), a present-day lithospheric thickness of 400-600 km (Khan et al., 2021), and moment of inertia and love number constraints, Huang et al. (2022) prefer a model with 10 to 15x crustal HPE enrichment and present-day average surface heat flow of 21 to 24 $\mathrm{mW/m^2}$, implying a relatively sluggish mantle with a reference viscosity of 10^{20}–10^{22} Pa s. The InSight-constrained geodynamic modeling of Samuel et al. (2021) favor 10x crustal enrichment, and orbital gamma ray spectrometry also supports an enrichment of ∼10-15x (Boynton et al., 2007; McLennan, 2001; Taylor et al., 2006).

In addition to the new results from InSight, geodynamic models must also be consistent with the observed volcanic history of Mars. Mars' volcanic history, as well as the present-day topography and gravity field, are dominated by the Tharsis rise, a broad dome 8000 km in diameter and 10 km high–far larger than any terrestrial igneous province–containing several large volcanoes, centered in the equatorial western hemisphere (Janle & Erkul, 1990). The origin of the Tharsis rise is generally ascribed to one or more long-lived mantle plumes (Carr, 1973; Harer & Christensen, 1996; Kiefer, 2003; Li & Kiefer, 2007). While most of the rise itself was emplaced by lava lows by the end of the Noachian, and the large volcanic shields in the Hesperian, the region has remained volcanically active for most of the planet's history (Phillips et al., 2001; Neukum et al., 2004; Richardson et al., 2017). According to Neukum et al. (2004), there is evidence of volcanism in Tharsis as recently as 2.4 million years ago. The relatively recent volcanic and tectonic activity, and modeled long-term stability of convection in the Martian mantle indicates that mantle melting is still occurring in the present day (Kiefer, 2003; Li & Kiefer, 2007; Kiefer & Li, 2016).

The Tharsis rise straddles the boundary between the thicker crust of the southern highlands and the thinner crust of the northern lowlands (Neumann et al., 2004). The contrast between these two hemispheres (zonal degree-1 topography) is referred to as the Martian crustal dichotomy. This feature is apparent in the hypsometry (elevation frequency distribution) of Mars, which has a bimodal distribution with peaks separated by 5.5 km (Aharonson et al., 2001; Watters & Schubert, 2007). The origin of the dichotomy is still highly uncertain. It may be of internal origin, for example the result of degree-1 mantle convection (Roberts & Zhong, 2006; Zhong, 2009), or from a giant impact (Andrews-Hanna et al., 2008; Kiefer, 2008; Marinova et al., 2008). A hybrid origin from degree-1 mantle convection caused by the giant impact has also been proposed (Citron et al., 2018). Several studies have considered a causal link between the dichotomy and Tharsis (S. King & Redmond, 2005; Šrámek & Zhong, 2012; van Thienen et al., 2006; Wenzel et al., 2004; Zhong, 2009). S. King and Redmond (2005) propose that Tharsis is the result of small-scale convection at the dichotomy boundary caused by the difference in crustal or lithospheric thickness.

However, there are other significant volcanic regions besides Tharsis, including the Elysium rise which is a smaller version of Tharsis but, still comparable in size to the largest igneous provinces on Earth. Unlike Tharsis, the Elysium rise itself and its volcanic shields appear to have had less recent volcanic activity than Olympus Mons and the Tharsis Montes associated with Tharsis swell, with a steep decline after a peak $\sim$1 Ga (Platz et al., 2010; Susko et al., 2017). However, the greater Elysium region shows evidence of more recent activity to the southeast of the rise, including volcanism within the past 0.2-20 Myr in Elysium Planitia, and in particular Cerberus Fossae (Susko et al., 2017; Horvath et al., 2021; Berman & Hartmann, 2002; Vaucher et al., 2009; Jaeger et al., 2010). Geophysical evidence also supports recent and presently active tectonism, possibly driven by magma, in Cerberus Fossae, as well a possibly active mantle plume beneath Elysium Planitia (Stähler et al., 2022; Broquet & Andrews-Hanna, 2022). Between Tharsis and Elysium lies the vast lava plain of Amazonis Planitia, produced by lava flows of the late, eponymous, Amazonian Period. Other, much older, volcanic regions of significance include the Syrtis Major province, as well parts of the Southern Highlands such as Tyrrhenus Mons and Hadriacus Mons (Hiesinger & Head III, 2004; Mouginis-Mark et al., 2022).

Geoid anomalies provide another constraint on the dynamics of planetary interiors (Hager et al., 1985; Roberts & Zhong, 2004; S. D. King, 2008). However, as Mars' gravity field and geoid are dominated by the topography of the Tharsis rise, largely built up by lava flows, removing or greatly reducing the effect of Tharsis from Mars' measured gravity field allows a much more useful comparison with our model geoids. Zuber and Smith (1997) calculated the low-degree (ℓ=2-6) coefficients for Mars without Tharsis (MWT), which we use for comparison–though this MWT geoid retains shorter wavelength features associated with Elysium, as well the large shields of Tharsis, as well as large impact basins such as Utopia and Hellas. (Spherical shell modeling does not include or produce the topography built up by lava or excavated by impacts.)

Using the 3D spherical shell geodynamic code CitcomS (Zhong et al., 2000; Tan et al., 2006; Zhong et al., 2008), we investigate the thermal and volcanic history of Mars. We consider runs successful if they are capable of producing: present-day temperature profiles (geotherms or potential temperatures) that fall within the range inferred from InSight results (Khan et al., 2021; Huang et al., 2022); geoid and topography power spectra consistent the the observations after removing the effect of Tharsis (Zuber & Smith, 1997), and sufficient melt in the first billion years to explain the widespread volcanism with isolated pockets of melt at present day. If the models are too hot, they will produce a persistent global melt layer lasting billions of years, while if they cool too quickly, melt production will be too low and end too early to be consistent with Mars. The observation of volcanic activity within the past 100 million, and even past few million years (Berman & Hartmann, 2002; Horvath et al., 2021; Jaeger et al., 2010; Neukum et al., 2004; Vaucher et al., 2009), means that acceptable models should produce small amounts of melt up to, or at least near, present-day.

Elysium is comparable in size to the largest terrestrial igneous provinces. Like Tharsis it also comprises a broad rise (2400 km $\times$ 1700 km) topped by large volcanoes and shows evidence for billions of years of volcanic activity–albeit not as recently as Tharsis, with a steep decline in volcanism after a peak $\sim$1 Ga (Malin, 1977; Platz et al., 2010; Susko et al., 2017). However, the greater Elysium region shows evidence of more recent activity to the south and southeast of the rise, including volcanism within the past 0.2-20 Myr in Elysium Planitia (the region where InSight landed), and in particular Cerberus Fossae (Susko et al., 2017; Horvath et al., 2021; Berman & Hartmann, 2002; Vaucher et al., 2009; Jaeger et al., 2010). Geodynamicists have typically focused on Tharsis, because Elysium and its three major volcanoes, while large by Earth standards, are markedly smaller than Tharsis and its largest volcanoes. Therefore, Martian volcanism has been modeled as a single long-lived plume (Harer & Christensen, 1996). The mantle convective structure in this one-plume model is represented by a sectoral degree-1 spherical harmonic, where the hemisphere containing Tharsis is dominated by upwelling from the plume and the other hemisphere is dominated by downwelling (Roberts & Zhong, 2006). Others, including Kiefer (2003); Li and Kiefer (2007); Kiefer and Li (2016), favor a multi-plume model for Tharsis. Instead of one very large plume, there would be a group of smaller plumes under Tharsis, each feeding one of the main volcanoes. Such plumes have been modeled as stable over billions of years and ongoing melt production at their centers would explain the continued volcanic activity over this time period, even to the present-day Li and Kiefer (2007).

2 Methods

2.1 CitcomS

We model the Martian mantle using a modified version of the finite element geodynamics code CitcomS (Zhong et al., 2000; Tan et al., 2006; Zhong et al., 2008). The solid mantle behaves as an extremely viscous fluid over long timescales, which is modeled as a creeping flow. CitcomS solves the following nondimensionalized equations for the conservation of mass, momentum, and energy, respectively:

$$\nabla \cdot \mathbf{u} = 0 \tag{1}$$

$$-\nabla P + \nabla \cdot \left[\eta \left(\nabla \mathbf{u} + \nabla^T \mathbf{u}\right)\right] + RaT\mathbf{e}_r = 0 \tag{2}$$

$$\frac{\partial T}{\partial t} + \mathbf{u} \cdot \nabla T = \nabla^2 T + Q \tag{3}$$

where $\mathbf{u}$ is the velocity, P is the pressure, η is the viscosity (temperature-dependent Newtonian), T is the temperature, $\mathbf{e}_r$ is the unit vector in the radial direction, and Q is an internal heat source (and/or sink). Ra is the Rayleigh number given by

$$Ra = \frac{\rho_m g \alpha \Delta T {R_p}^3}{\kappa \eta_0}, \tag{4}$$

where ρ_m is the average mantle density, g is the gravitational acceleration, α is the coefficient of thermal expansion, ΔT is the initial super-adiabatic temperature difference across the mantle, R_p is the planet's radius, κ is the thermal diffusivity, and η_0 is the mantle reference viscosity. Table 1 shows the values we use for these and other parameters. An important note here for comparing CitcomS results with other work is that the Rayleigh number is usually defined by a layer thickness, D, however CitcomS uses, R_p, the radius of the planet, for the length scale instead. For efficiency, CitcomS computations are parallelized (Tan et al., 2006). We model incompressible flow using the Boussinesq approximation.

We have made several changes and additions to the CitcomS code. The original code keeps mantle internal heating constant through time. However, because heat production results from the decay of radioisotopes, it is more realistic to have it decrease accordingly using the calculations described by Turcotte and Schubert (2014). Crustal enrichment of radioisotopes has also been added. We have incorporated the cooling of the planet's core, which is treated based on the coupled core and mantle thermal evolution model developed by Stevenson et al. (1983) As the core cools, the heat from the core heats the mantle from below, while the core-mantle boundary (CMB) temperature decreases.

2.2 Melt production

The largest modification to CitcomS is the incorporation of melting calculations. Much of the work on melting in Mars' mantle (Li & Kiefer, 2007; Kiefer, 2003; Kiefer & Li, 2016; Ruedas et al., 2013) was performed in 2D spherical axisymmetric geometry (or 2D Cartesian in the case of Tosi et al. (2013)) rather than 3D. With the exception of Ruedas et al. (2013), these also do not consider the decrease in radioisotope abundances through time or the thermodynamics of core cooling and solidification. Spherical 3D modeling incorporating decaying heating as well as crustal enrichment of radioisotopes has become more common over the past few years (Sekhar & King, 2014; Plesa et al., 2016, 2018). Because the melting formulation is new to CitcomS, we describe it in some detail below.

The first step in melt calculations is to calculate the equilibrium melt fraction, which for a given composition is a function of temperature and pressure. We calculate melt fraction (by mass) using the empirically derived parameterization of Katz et al. (2003) for dry peridotite melting at upper mantle pressures. We convert this mass fraction to a volume fraction given the solid mantle density (herein $3500\,\mathrm{kg\,m^{-3}}$) and the presumed melt density ($3000\,\mathrm{kg\,m^{-3}}$). The melt fraction algorithm of Katz et al. (2003) was developed by fitting experimental data on equilibrium melting of peridotite and is valid up to approximately 8 GPa. Katz et al. (2003) has since found broad application in geodynamic mantle convection codes such as CitcomS (e.g., Citron et al. (2018); Šrámek and Zhong (2012)), as well as ASPECT and adaptations thereof (e.g., Dannberg and Heister (2016)). While Katz et al. (2003) was originally published with terrestrial melting in mind, it has been applied to calculate melt productivity in convection models of the Martian mantle by Citron et al. (2018), Kiefer and Li (2016), and Šrámek and Zhong (2012). According to Šrámek and Zhong (2012) and Kiefer and Li (2016), the Katz et al. (2003) solidus is close to experimentally derived Mars solidi, such as those of Bertka and Holloway (1994); Agee and Draper (2004); Matsukage et al. (2013), using inferred Martian mantle compositions. The utility of Katz et al. (2003) is that it includes a solidus, liquidus, and a relatively straightforward nonlinear way to calculate melt fraction. Earlier geodynamic modeling employed simpler methods, such as Kiefer (2003) linearly increasing melt fraction between the solidus and assuming the liquidus is a fixed temperature above the solidus. We use the liquidus and lherzolite liquidus of Katz et al. (2003) for dry peridotite. However, we replace their solidus with that of Duncan et al. (2018). The Katz et al. (2003) solidus in degrees Celsius as a function of pressure P in GPa, 1085.7 + 132.9 P - 5.1 P^2, is higher than the Mars solidus of Duncan et al. (2018), 1088 + 120.2 P − 4.877 P^2 by up to 45°C (at 4 GPa) in the range of depths in which our models produce melt (see Figure 2).

The melt fraction by mass obtained from this modified katz2003new method is then converted to a fraction by volume according to the equation

$$X_{vol} = \frac{\rho_s}{\rho_m \left(\frac{1}{X_{mass}} - 1\right) + \rho_s} \tag{5}$$

where X_{vol} is the melt fraction by volume, X_{mass} is the melt fraction by mass, ρ_s is the solid mantle density ($3500\,\mathrm{kg\,m^{-3}}$, and rho_m is the melt density ($3000\,\mathrm{kg\,m^{-3}}$). From this point on, the melt fraction X refers to the volume fraction.

Melt production computations must consider not only the portion of a region that is molten (melt fraction), but also the movement of the mantle material through the melting region. Based on equation B1 of Watson and McKenzie (1991), $\dot{M}$, the instantaneous amount (herein, volume) of melt per unit (volume) of mantle material produced per unit time, is the material derivative of the equilibrium melt fraction X (by volume),

$$\dot{M} = \frac{DX}{Dt} = \frac{\partial X}{\partial t} + \mathbf{u} \cdot \nabla X. \tag{6}$$

Using the chain rule, $\dot{M}$ can be written in terms of the partial derivatives of melt fraction with respect to temperature and pressure.

$$\dot{M} = \frac{DX}{Dt} = \frac{\partial X}{\partial T}\frac{DT}{Dt} + \frac{\partial X}{\partial P}\frac{DP}{DT} = \frac{\partial X}{\partial T}\left(\frac{\partial T}{\partial t} + \mathbf{u} \cdot \nabla T\right) + \frac{\partial X}{\partial P}\left(\frac{\partial P}{\partial t} + \mathbf{u} \cdot \nabla P\right) \tag{7}$$

Assuming $\partial P/\partial t$ is zero and pressure is hydrostatic, then

$$\dot{M} = \frac{\partial X}{\partial T}\left(\frac{\partial T}{\partial t} + \mathbf{u} \cdot \nabla T\right) - \frac{\partial X}{\partial P}\bar{\rho} g u_r \tag{8}$$

where u_r is the radial component of velocity, and $\bar{\rho}$ is the radial profile of density. The volume of melt produced is calculated by integrating $\dot{M}$ over the element volumes using Gaussian quadrature.

2.3 Model cases

2.3.1 Rheology

We start by modeling a structural reference case, with a uniform lithosphere thickness rather than a hemispheric dichotomy. We run 18 models with this "uniform" structure, testing three values each for the initial CMB temperature (1720 K, 1870 K, 2020 K) and crustal HPE enrichment factor (5x, 10x, 15x), and two values for the activation energy E* ($117\,\mathrm{kJ\,mol^{-1}}$, $350\,\mathrm{kJ\,mol^{-1}}$). The initial HPE concentrations are derived from the present-day bulk concentrations from Wänke and Dreibus (1994) (Table 1), projected back in time. Based on Christensen (1983), activation energy is divided by the stress exponent n to approximate a power law rheology for olivine. Typically n is taken to be 3, but we vary the effective activation energy, corresponding to testing values of n=3 (dislocation creep) and n=1 (diffusion creep). Thus to approximate n=3, the nominal activation energy of $350\,\mathrm{kJ\,mol^{-1}}$ becomes $117\,\mathrm{kJ\,mol^{-1}}$ (low activation energy cases), while for n=1, we keep the activation as $350\,\mathrm{kJ\,mol^{-1}}$ (high activation energy cases).

The temperature and pressure (depth) dependent viscosity η is given, in dimensional form, by

$$\eta = A \cdot \eta_0 \cdot \exp\left(\frac{E_a + PV_a}{RT} - \frac{E_a + PV_a}{R(\Delta T + T_s)}\right) \tag{9}$$

where η_0 is is the reference viscosity ($1.0 \times 10^{21}\,\mathrm{Pa\,s}$), E_a is the activation energy (either 117 or $350\,\mathrm{kJ\,mol^{-1}}$), P is the pressure, V_a is the activation volume ($6.6\,\mathrm{cm^3\,mol^{-1}}$), R is the ideal gas constant, and T is the absolute potential temperature. The pre-exponential factor A is to control the viscosity by layer. To enforce a strong (initially 100 km thick) lithosphere, from the surface to 100 km depth, A = 10. From 100 km to 1000 km depth, A = 0.1, establishing a weak asthenosphere. From 1000 km depth to the CMB, A = 10, accounting for a strong transition zone rheology.

2.3.2 Temperature initial condition

The initial mantle temperature profile is set to a uniform temperature T_m (here, ΔT = 1500K) everywhere with cold and hot thermal boundary layers are added at the top and bottom, respectively. Small magnitude (0.01 ΔT) spherical harmonic degree 8, order 6 perturbations are added at all layers to initiate convection. The boundary layer temperatures are calculated by adjusting T_m based on 1D conductive cooling (at the top) or heating (bottom) of a half-space after a "half-space age". The top boundary layer is thus achieved by adjusting the constant temperate profile according to:

$$T(r) = T_m - (T_m - T_{surf}) \cdot \text{erf}\left(\frac{R - r}{2\sqrt{(a)}}\right) \tag{10}$$

and similarly the bottom boundary layer is created by

$$T(r) = T_m + (T_{cmb} - T_m) \cdot \text{erf}\left(\frac{r - r_{cmb}}{2\sqrt{(a)}}\right) \tag{11}$$

where $T(r)$ is the initial temperature at radius r, T_{surf} is the surface temperature (220 K), T_{cmb} is the initial CMB temperature, R is the radius of the planet (3389.5 km), r_{cmb} is the radius of the CMB, and a is the conductive cooling/heating age of the half-space. For all 18 uniform structure cases, The initial error function temperature profile, with top and bottom boundary layers, is based on a half-space age of 100 Myr.

2.3.3 Geoid Comparison

We compare the power spectrum of each of the geoids output by our models to the power spectrum of the observed Martian geoid with the effect of Tharsis' low degree ($\ell \leq 6$) topography removed, i.e. Mars without Tharsis (MWT), as determined by the spherical harmonic gravity coefficients of Zuber and Smith (1997). We calculate the normalized root mean square error (NRMSE) of the model geoid power spectrum from spherical hamronic degrees ℓ = 2–6, given by

$$NRMSE = \sqrt{\frac{\sum_{\ell=2}^{6} \left(P_{\text{MWT},\ \ell} - P_{\text{model},\ \ell}\right)^2}{\sum_{\ell=2}^{6} {P_{\text{MWT},\ \ell}}^2}} \tag{12}$$

where ℓ is the spherical harmonic degree, $P_{\text{MWT, l}}$ is the power in degree ℓ of the MWT geoid, $P_{\text{model, l}}$ is the power in degree ℓ of the model geoid. (The mean squared error is normalized by the mean of the squared values for MWT, and the numbers of points n = 5, cancel.) In this formulation, a geoid identical to MWT would have an NRMSE of 0, and a geoid with zero power for ℓ = 2–6 would have an NRMSE of 1.

2.3.4 Dichotomy

We repeat the range of nine high activation energy cases (3 crustal enrichments, 3 initial CMB temperatures) for models with a degree-1 hemispheric dichotomy structure (boundary along the equator). As opposed to the uniform cases described above, these are the nine "dichotomy" cases. The initial error function temperature profile in the southern hemisphere for these dichotomy cases is based on a thermal half-space age of 500 Myr. The initial temperature profile in the northern hemisphere is based on a thermal age of 100 Myr, as would result from the dichotomy-forming impact resetting the temperature profile ∼400 Myr after Mars formed. The initial southern hemisphere lithosphere is correspondingly set 100 km thicker than the northern hemisphere lithosphere by setting the viscosity in the lid to the maximum allowed value (as applied when truncating very high viscosities), which for our models is $10^5\eta_0 = 1 \times 10^{26}$ Pa s.

3 Results

3.1 Overview

Of the three parameters we varied (activation energy, crustal HPE enrichment, and initial CMB temperature), the results are most sensitive to the activation energy, and generally least sensitive to the CMB temperature. Therefore, the plots in the figures are grouped first by activation energy, specifically by the value of the stress exponent n that the nominal activation energy (350 $\mathrm{kJ\,mol^{-1}}$) is divided by in order to vary the effective activation energy. Above the bottom thermal boundary layer, the mean mantle temperatures and mean radial temperature profiles (geotherms) are not strongly influenced by the initial CMB temperature. Higher activation energy and, to a lesser degree, lower crustal enrichment and the the thicker southern lithosphere of the dichotomy cases, lead to a overall hotter mantle. However, these higher activation energies, and thus higher temperatures in the lower to mid-mantle, are reached with a thicker upper thermal boundary layer. As a consequence of the higher average temperatures they produce, lower enrichment and higher activation energy lead to more melt being produced for longer, in many cases nearly to the present day. Melting occurs primarily in the middle of the heads of plumes or the linear upwellings like those in Figure 5 (d) and (e). No inner core forms in any of our models, consistent with the InSight results constraining at most a very small, or, more likely, no inner core (Stähler et al., 2021; Irving et al., 2023).

3.2 Mantle Temperature and Geotherms

Figure 3 (a–c) shows the mean potential temperature profiles, or geotherms, at the time corresponding to present day for all the models, in three separate plots grouped according to the rheology: uniform structure, low activation energy; uniform structure, high activation energy; and dichotomy, high activation energy. On each of these three plots, the 1605 ± 100 K mid-mantle temperature from Huang et al. (2022) is marked by the vertical magenta lines, with the minimum and maximum dashed. The range of geotherms from the models of Smrekar et al. (2019) is shaded, with the lighter shading being below the mean, and the darker shading above it. All of the low activation energy geotherms fall several hundred kelvins below both Huang et al. (2022) and Smrekar et al. (2019). The mid-mantle temperatures for all high activation energy cases, including those with the dichotomy, plot within the range of Huang et al. (2022). The 5x and 10x enrichment cases also fall within the range of Smrekar et al. (2019), as do the 15x cases at depths less than $\sim$750 km. Our geotherms, not unlike Huang et al. (2022), are generally on the cooler side of the range of Smrekar et al. (2019), although they have a somewhat different shape such that the for depths between $\sim$100 and $\sim$500 km, the high activation energy cases with 5x and 10x enrichment rise above the mean of Smrekar et al. (2019).

The time evolution of the mean mantle potential temperature is likewise plotted in Figure 3 (d–f). The cases with lower crustal enrichment, that is those which retain more of the HPE in the mantle, heat up over the first few hundred million years as a result of this radiogenic heat. With the low activation energy rheology, this effect is only notable with the 5x enrichment, and even then very subtle. For high activation energy, this occurs with similar subtlety in the 10x cases, albeit stretched out over a longer time so that the peak temperature is later. Whereas the temperature increase with 5x enrichment is more pronounced and the peak $\sim$200-300 Myr later, which would be near the beginning of the Hesperian. With adding the dichotomy, the timing of the peak temperature is later still at about 3200 Ma, well into what would be the Hesperian.

Across all of our 27 cases, the mean present-day surface heat flux only ranges from 12.3 $\mathrm{mW\,m^{-2}}$ (high activation energy, enrichment = 5x, initial T_{CMB} = 1720 K) to 14.1 $\mathrm{mW\,m^{-2}}$ (low activation energy, enrichment = 5x, initial T_{CMB} = 2020 K). Of note, these values are only about half of the heat fluxes modeled by Plesa et al. (2015) and Plesa et al. (2016). Our mean surface heat fluxes correlate positively with initial CMB temperature, and negatively with activation energy. For high activation energy, the fluxes also increase with crustal enrichment, but curiously for low activation energy, the minimum surface heat flux occurs with 10x enrichment across all three initial CMB temperatures.

3.3 Geoids

The power spectra (from spherical harmonic degree ℓ=2–20) of the present-day geoids output by our models are plotted in Figure 4, with MWT in blue on each subplot. The NRMSE values for all 27 model power spectra are tabulated in Table 2. In terms of matching the MWT geoid power spectrum from $\ell = 2$–6 (i.e., having a lower NRMSE), the uniform structure, low activation energy, 15x enrichment cases have a remarkably good fit. (Though, to reiterate, the geotherms of these models fall well outside our constraint.) Several of the uniform, high activation cases, which do meet our geotherm constraint, also have a geoid that deviates relatively little from MWT, including all of the 10x enrichment cases and the 5x enrichment case with the hottest (initially 2020 K) CMB. For the uniform structure, the low activation energy cases with 5x enrichment, and the coolest (1720 K initial CMB) 10x enrichment case, have the poorest fits (high NRMSE) with MWT. Whereas for the uniform, high activation energy cases, it is the three 15x enrichment cases, and the coolest (1720 K initial CMB) 5x enrichment case, that have the poorest fits with MWT. Thus, broadly speaking, for low activation energies, the geoids of the 15x enrichment cases are favored, while for higher activation energies (without the dichotomy), the 10x enrichment cases are generally favored.

Turning to the dichotomy models (high activation energy only), there is less of a pattern in how well the geoids fit MWT, other than that the 5x enrichment cases are almost as poor at matching MWT as the 5x enrichment low activation energy cases without the dichotomy. In contrast to those well-fitting uniform, low activation energy, 15x enrichment cases, the hottest (2020 K initial CMB) 15x enrichment dichotomy case has the second poorest fit with MWT of all 27 models. Among the dichotomy cases, the hottest (2020 K initial CMB) 10x enrichment case best matches MWT, although the intermediate temperature (1870 K initial CMB) 15x enrichment case is still a relatively good fit.

3.4 3D Mantle Structure Evolution

All of the models develop long-lived plumes or plume-like linear upwellings. The cases without the dichotomy, both for low and high activation energies, tend to first develop a convection pattern dominated by degree-2, with two large antipodal plumes, but connected by a less prominent linear upwelling (Figure 5 (a, b)). This pattern gradually evolves into a persistent pattern dominated by a single linear upwelling that curves around much of planet–in some cases encircling it as a sinuous ring (Figure 5 (d, e, g, h)). When the upwelling remains discontinuous, one or both ends of the linear upwelling are warmer, with a broader head, where there is greater melting (Figure 5 (d, g)). The dichotomy models behave very differently. Within a few hundred million years they develop a degree-1 structure comprising a single large plume centered on the pole of the northern hemisphere–the one with thinner lithosphere and the warmer (younger) half-space initial temperature profile. Unlike the initially imposed step in lithospheric thickness–which gradually smooths out–this degree-1 convection pattern persists through present-day; although the plume becomes less vigorous as it, like the mantle as a whole, cools. While Mars is sometimes thought of as a 'one plume planet', the single upwelling plume is often assumed to form beneath the southern highlands and migrate toward the equatorial region (Zhong, 2009; Sekhar & King, 2014).*other cites here.* There is no geologic evidence supporting a plume forming beneath the Northern highlands and migrating to the south.

3.5 Melting

The total amount of melt over time, represented as the fraction of the mantle's volume that is molten (e.g., 0.1 = 10% of the mantle is melt) plotted in Figure 6 (a-e). This bulk melt fraction generally follows the trend of the mean mantle temperature, peaking after a few hundred million years, and then declining over the rest of the model run. The low activation energy cases, and the high activation energy cases with 10-15x enrichment and a cooler CMB, do tend to have an additional, earlier peak within the first 100 Myr, in some cases at the initial time step. In the cases with 15x enrichment and the initial CMB temperature of 1720 K, there is only this one early peak, corresponding with the rising of plumes.

The melt fraction in all models peaks with the mantle being at least several percent melt, with the 5x enrichment cases reaching bulk melt fractions well over 10%. All melting in our models occurs within a relatively narrow range of pressures/depths (2.6-4 GPa / ∼200–300 km) in the upper mantle, and the local melt percentages here can reach in excess of 40-50% by volume. The bulk melt fraction steadily drops after the early peak so that by ∼2000 Ma in the low activation energy cases and by ∼500-1000 Ma in the high activation energy cases, there is no discernible melt on the linear scales of Figure 6 (a–c). But this is in part misleading; a small mount of melt remains, in many cases persisting up to or near the present day, and this is more visible when the bulk melt fraction is plotted on a logarithmic scale as in Figure 6 (d–f). The overall amount of melt produced is not significantly affected by adding the dichotomy to the high activation energy cases, though it is marginally reduced.

The cases with low activation energy show much less spread in their melt production over time than the high activation energy cases when varying the enrichment and initial CMB temperature. Put another way, models with high activation energy are more sensitive to changes in the other parameters we varied. The coldest (15x enrichment) high activation energy models produce less melt through time than even the coldest low activation energy models, while the hottest (5x enrichment) high activation energy cases produce more melt than all of the low activation energy models. Each 5x and 10x enrichment case produces a melt volume within or above the nominal volume of the Tharsis rise (lighter gray shading in Figure 6, as does the low activation energy 15x enrichment case with the hottest (initially 2020 K) CMB. Yet, only the single warmest case of all 27 cases–the high activation energy, uniform structure model with 5x enrichment and the hottest (initially 2020 K) CMB–produces enough melt for Tharsis when accounting for limited extraction of mantle melt to the surface (darker shading in Figure 6).

Even on the logarithmic scale, the time of last melting is not clear from Figure 6, because the latest bulk melt fraction is more than 10 orders of magnitude lower than the peak. The precise model time and corresponding age of last melt production for each model case is listed in Table 3. Many cases are still producing melt at the end of the run, at present-day, and in others melting has only cut off within the past few hundred million years. These tend to be the lower enrichment cases. In all of the uniform 15x enrichment cases, melting shuts off well over 1 Ga. Melt continues for longer in the dichotomy 15x enrichment cases, even up to present day in the case of the hottest (initially 2020 K) CMB. Still not clear from either Figure 6 or Table 3 is that several models, mostly 10x enrichment cases, see melt production stop and restart one or more times before finally ending, or reaching present-day with melt present. These last trickles of melting are very small and localized.

4 Discussion

4.1 Model Summary

Of the three parameters varied (activation energy, crustal HPE enrichment, and initial CMB temperature), the results are most sensitive to the activation energy. The results are least sensitive to the initial CMB temperature. Higher activation energies, and thus higher temperatures in the lower to mid-mantle, result in a cooler and thicker lid, but also an overall hotter mantle. Corresponding with the higher average temperatures, lower enrichment and higher activation energy lead to more melt being produced for longer. The cases with a hotter CMB, and a cooler mantle due to lower concentrations of HPEs (higher crustal enrichment) are more influenced by bottom heating. In these cases, more vigorous plumes that rise at the beginning of the model run contribute more directly to the melting.

The results summarized and color coded in Figure 7 show whether each of our 27 model cases fits our constraints for (1) geotherms consistent with InSight results, (2) recent production of melt, (3) sufficient melt to produce Tharsis, and (4) matching the MWT geoid. Blue indicates the constraint is met, and red that it is not. Purple indicates an intermediate result (geoids) or that the constraint is met with qualification. For the geotherms, blue models have a mid-mantle temperature that falls within the 1605±100 K range of Huang et al. (2022), and red models fall well outside this range. For melt at present-day, models where melt is present at 4500 Myr into the run (0 Ma) are blue, and those with no melt in the past 200 Ma are red. The last melt in purple models occurs between 200 Ma and present-day, which given the limited resolution and high uncertainty in these models, could still be consistent with geologically recent melt. For melt volume production, blue models produce at least 1×10^9 of melt–sufficient to produce the Tharsis rise with 10% extraction. Red models produce $< 1\times10^8$ of melt, which is the minimum needed for Tharsis with 100% extraction. Purple models produce a total melt volume between these values, sufficient for Tharsis if melt extraction is $>$ 10%. For the geoids, an NRMSE (Table 2) $<$ 0.6 is blue; 0.6 $\leq$ NRMSE $<$ 0.8 is purple, and NRMSE $\geq$ 0.8 is red.

Figure 7 shows that overall, the model cases most consistent with our constraints for Mars are the high activation energy cases with 5-10x crustal HPE enrichment, and more so the uniform structure cases than the dichotomy cases. The very cold geotherms of all nine low activation energy cases lead us to reject that rheology in favor the high activation energy rheology. The few examples in which a low activation energy case fully satisfies our constraint in any one category (blue) diverge, in that only a couple of 5x enrichment cases have melt at present-day, while it is the three low activation energy, 15x enrichment cases that produce geoids consistent with MWT. Indeed two of those three geoids are the best fits of all 27 models.

4.2 Geoids

Our models can only address the mantle contribution to the geoid, while the actual Martian geoid is also determined in part by crustal thickness and possible density anomalies within the crust. It is generally considered that lower spherical harmonic degrees of the geoid are dominated by the mantle, while higher degrees are dominated by the crust. Yet, in the case of Mars, the thickened crust of Tharsis dominates the lowest degrees of the geoid. Using the geoid obtained from the MWT gravity coefficients of Zuber and Smith (1997) to remove Tharsis, up to and including ℓ=6, mitigates the crustal contribution issue, such that we consider the crustal contribution negligible through ℓ=6. Furthermore, for l¿∼12, the geoid should be almost entirely determined by the crust. At the intermediate degrees, the crustal and mantle components should both be significant, and ideally we could separate these two and compare out model geoids with just the mantle component. However, resolving the question of these crustal contributions to the geoid is beyond the scope of this work, and we focus on the fit of our models with MWT through ℓ=6.

A subset of our models–particularly those with a uniform structure, high activation energy, and 5–10x enrichment–which meet our geotherm and melting constraints also meet our MWT geoid constraint. All three low activtion energy, 15x enrichment cases meet the geoid constraint as well. Indeed, these three include the geoid power spectra with the two lowest NRMSE values of all out models. Still, these three models perform unacceptably in that they cool far too quickly to meet our geotherm or present melt constraints.

4.3 Melting and Thermal Evolution

Many of our models produce a small amount of melt up to or near present-day, with some cases having small amounts of melting stopping and restarting. This is consistent with small, localized pulses of volcanism on Mars within the past few million to $\sim$100 million years. It should be noted that our models have limited resolution, for example $\sim$25 km vertical resolution, and still lower in the lateral direction over most of the mantle, including the 200-300 km melting depths. Therefore, it is possible that were these same parameters and initial conditions run at a significantly higher resolution–which would take an infeasible amount of computing time and power–melting could continue for a little longer, and would not stop and restart.

Producing sufficient melt for Tharsis while also producing a geoid power spectrum that is consistent with present-day Mars without the volcanically constructed topography of Tharsis (i.e., MWT) is very difficult. It is even difficult just to produce enough melt to account for the enormous volume of Tharsis, while also considering that only a fraction of melt produced in the mantle erupts on the surface. As depicted in Figure 7, only our single hottest case (high activation energy, 5x enrichment, 2020 K initial CMB temperature) fully fulfills our constraint assuming 10% melt extraction–and then only barely. (This case, alone among all nine 5x enrichment cases, satisfies our geoid constraint.) Yet this singular case still does not produce this quantity of melt quickly enough to allow for emplacement of the Tharsis rise by the late Noachian. The majority of our cases–and every case with 5-10x enrichment–produce at least a Tharsis-equivalent melt volume within the mantle, but this could only account for Tharsis if the majority (60%) of that melt were extracted to the surface.

We find the present-day geotherms from our models with the high activation energy rheology to be very consistent with present day Mars, while the geotherms of the low activation energy are hundreds of degrees colder than inferred from the results of InSight and previous modeling. It is, however, remarkable that despite the cold mean geotherms, the 5x enrichment cases with this low activation energy rheology are able to locally produce small volumes of melt up to or near present-day. The large discrepancy in geotherms does lead us to broadly reject the low activation energy rheology, so much so that this was not considered when modeling the dichotomy.

With regard to crustal HPE enrichment, and rather unsurprisingly, Figure 7 also reflects how the melting results favor lower crustal enrichment, which is somewhat at odds with the body of work favoring 10-15x enrichment–as well as the the geoid power spectra of our models. Nevertheless, most of the 10x cases with high activation energy produce melt up to or near present-day, and up to about ℓ=6 the geoid is a good fit with MWT. The 10x enrichment cases do produce significantly less melt overall, and early on, compared to the 5x cases. But even the 5x enrichment cases cannot produce enough melt, at least not quickly enough, to account for Tharsis without extremely efficient melt extraction.

The present day geotherms from the low activation energy cases are hundreds of degrees too cold to be consistent with what has been inferred for Mars, therefore we generally prefer the models with the higher activation energy. Nevertheless, the models with low activation energy and 15x enrichment provide the best-fitting geoid to observations. The power spectra for the 10x and 15x enrichment, high activation energy cases do still match well with the MWT geoid up to ℓ=6–8. Only at higher degrees is there significantly less power in the geoid for these cases compared to MWT, and the low activation energy 15x enrichment cases.

We do not consider in our modeling initial conditions arising from a magma ocean overturn (Elkins-Tanton et al., 2003; Elkins-Tanton, 2005). One might speculate that this would stabilize the mantle with regard to convection for some period of time, allowing the mantle to heat up. The interaction of the two effects of (1) cooling the mantle due to the overturn, and (2) the subsequent heating of the mantle due to stabilizing the mantle against convection, make it difficult to predict the impact of this condition without further analysis. That is beyond the scope of this work.

4.4 Effects of Adding the Dichotomy

Because of the large mismatch in geotherms with the low activation energy cases, and the associated difficulty in generating sufficient melt, we only ran the dichotomy cases with high activation energy. To first order, the geotherms of the dichotomy cases are very close to those of the corresponding cases without the dichotomy. In the long term, the mantle temperature is much more sensitive to crustal enrichment than it is to the initially thicker southern lithosphere and warmer northern hemisphere mantle. Recall that the initial temperature profile is also different with the dichotomy cases. The start time is taken to be 4100 Ma instead of 4500 Ma as in the uniform cases. To account for this, we initialize the southern hemisphere with an error function temperature profile corresponding to an age of 400 Ma (versus 100 Ma for the uniform case). The northern hemisphere initial condition is kept as a profile corresponding to an age of 100 Ma, consistent with a younger lithosphere and a large injection of heat from the putative large impactor responsible for the dichotomy (Marinova et al. (2008); Kiefer (2008); Andrews-Hanna et al. (2008)). The geoid power spectra produced by the dichotomy cases are often a poorer match to MWT than the corresponding uniform, high activation energy cases. The exceptions to this trend, in which the dichotomy improves the geoid fit, are either relatively minor (10x enrichment, 2020 K initial CMB) or among the 15x enrichment cases that we reject for not meeting other constraints. Including the hemispheric dichotomy also marginally decreases the cumulative melt production. However, the initially thicker southern lithosphere does make it easier to maintain a small amount of melt close to present-day, and this is not wholly attributable to the later start time with the same initial temperature profile in the northern hemisphere. That said, at best, adding the hemispheric dichotomy does not significantly improve the overall fitting of our constraints. We therefore still prefer the uniform cases.

5 Conclusions

Overall, we find that our results from the model cases with a high activation energy rheology, uniform structure (i.e., without the dichotomy), and 5–10x crustal HPE enrichment are the most consistent with the data we have for Mars from InSight and earlier missions. To a lesser degree, our results also favor the cases among these six with initial CMB temperature of 1870-2020 K (i.e., greater than the initial mid-mantle temperature), in that those are the cases without any red in Figure 7. That said, model results are least sensitive to the initial CMB temperature, as compared to the activation energy and crustal enrichment. This is good, in that the early CMB temperature is one of the most difficult parameters to constrain. Several of the dichotomy cases are almost as consistent with our constraints (i.e., blue or purple across Figure 7) and even maintain melt a little longer than the corresponding uniform cases. But both the geoid fit to MWT and the cumulative melt production for the 5–10x enrichment are made worse by adding the dichotomy. Therefore, we don't consider the dichotomy, at least as we model it, to be necessary or overall useful in fitting our constraints for Mars.

The present-day geotherms from our model cases with the high activation energy are all consistent with Huang et al. (2022) in supporting a present-day mantle cooler than most pre-mission estimates by Smrekar et al. (2019), and the 10x enrichment geotherms align with the middle of the 1605±100 K range. Among our preferred cases, cumulative and present-day melt production slightly favor the 5x enrichment cases over the 10x cases. But even with 10x enrichment, the Martian mantle is still capable of producing small amounts of melt near or at present-day, and neither the 5x nor 10x enrichment cases produce sufficient melt for Tharsis quickly enough without assuming a majority of mantle melt is extracted. A 10x crustal enrichment factor would be consistent with the modeling and seismic analysis of Drilleau et al. (2022), the geodynamic modeling of Samuel et al. (2021), and the lower end of the range inferred by Huang et al. (2022). A 10x enrichment factor also agrees well with the orbital gamma ray spectrometry data that indicate ∼50% of Mars' HPE are contained within its crust (Boynton et al., 2007; McLennan, 2001; Taylor et al., 2006). Furthermore, the geoid power spectra for $\ell = 2$–6, for all three uniform, high activation energy, 10x enrichment cases are in good agreement with the MWT geoid derived from Zuber and Smith (1997). Modifying the radial viscosity structure of these 5–10x enrichment models may further improve the poorer fit at higher degrees up to $\ell \approx 12$, above which crustal structure, rather than the mantle we model, should overwhelmingly dominate the geoid.

It is challenging to reconcile such a cool mantle at present with the amount of melting required throughout–and particularly early on in Martian history. It is nevertheless reassuring that our models, and thus a mantle as cool as Huang et al. (2022) find for present-day Mars, are still capable of producing small, localized amounts of melt, as the evidence of recent volcanism (Neukum et al., 2004; Susko et al., 2017; Horvath et al., 2021; Berman & Hartmann, 2002; Vaucher et al., 2009; Jaeger et al., 2010) necessitates, and the ongoing tectonic activity in Elysium observed by InSight (Stähler et al., 2022; Perrin et al., 2022; Broquet & Andrews-Hanna, 2022; Kiefer et al., 2023) suggests. Melt production is very sensitive to the mantle temperature, or more precisely the portion of the mantle that is above the solidus. Therefore more melt in the late pre-Noachian to early Hesperian, as is necessary to produce the Tharsis and Elysium rises, requires a hotter mantle and/or a lower solidus. A hotter mantle would have to cool more quickly in order to still reach the cool observed geotherms. The faster cooling of a hotter mantle may be facilitated by the consequently more vigorous convection, and considering the effect of compressible convection and, in particular, the latent heat of melting. Alternatively, or in addition to this, including the effect of water or CO_2 could depress the solidus enough to significantly increase melt production at a given temperature.

Data/Software Availability Statement

[For the purposes of peer review, our modified CitcomS code, the model output used to create the figures in this manuscript, and a README describing the contents are temporarily available via the following private Figshare link: `https://figshare.com/s/f667c63d0392cc47367b`. Note that this is a nearly 1 GB .zip file.] We use our own custom modifications to the geodynamic code CitcomS version 3.3.1 (Zhong et al., 2000; Tan et al., 2006; Zhong et al., 2008), the official code of which is available from Computational Infrastructure for Geodynamics (CIG) at `http://geoweb.cse.ucdavis.edu/cig/software/citcoms/`, as well as `https://doi.org/10.5281/zenodo.7271920`, or on GitHub at `https://github.com/geodynamics/citcoms`. Our modified CitcomS code, input (.cfg) files, and output files at 500 million year intervals will be made available at `https://data.lib.vt`

`.edu/`. Line plots were made with Matplotlib version 3.5.1 (Hunter, 2007), available under the Matplotlib license at `https://matplotlib.org/` or at `https://doi.org/10.5281/zenodo.5773480` . 3D plots were made with Paraview version 5.9.0 (Ahrens et al., 2005), available from `https://www.paraview.org/`. For working with the geoid output and data, we use pyshtools (Wieczorek & Meschede, 2018), with documentation and installation instructions available at `https://shtools.github.io/SHTOOLS/`.

Acknowledgments

This paper is InSight Contribution Number 333. S.D.K. And J.P.M. were funded by NASA InSight Participating Scientist Program grant #80NSSC18K1623.

References

Agee, C. B., & Draper, D. S. (2004). Experimental constraints on the origin of Martian meteorites and the composition of the Martian mantle. *Earth and Planet. Sci. Lett.*, *224*, 415–429. doi: https://doi.org/10.1016/j.epsl.2004.05.022

Aharonson, O., Zuber, M., & Rothman, D. (2001). Statistics of Mars' topography from the Mars Orbiter Laser Altimeter: Slopes, correlations, and physical models. *J. Geophys. Res.*, *106*, 23723-23735. doi: https://doi.org/10.1029/2000JE001403

Ahrens, J., Geveci, B., & Law, C. (2005). ParaView: An end-user tool for large data visualization. In *Visualization handbook.* Elesvier. (ISBN 978-0123875822)

Andrews-Hanna, J., Zuber, M., & Banerdt, W. (2008). The Borealis basin and the origin of the martian crustal dichotomy. *Nature Lett.*, *453*(26), 1212-1215. doi: https://doi.org/10.1038/nature07011

Banerdt, W. B., Smrekar, S. E., Banfield, D., Giardini, D., Golombek, M., Johnson, C. L., ... others (2020). Initial results from the InSight mission on Mars. *Nature Geosciences*, *13*, 183-189. doi: https://doi.org/10.1038/s41561-020-0544-y

Berman, D. C., & Hartmann, W. K. (2002). Recent fluvial, volcanic, and tectonic activity on the Cerberus plains of Mars. *Icarus*, *159*(1), 1–17. doi: https://doi.org/10.1006/icar.2002.6920

Bertka, C. M., & Holloway, J. R. (1994). Anhydrous partial melting of an iron-rich mantle I: subsolidus phase assemblages and partial melting phase relations at 10 to 30 kbar. *Contributions to Mineralogy and Petrology*, *115*, 313–322. doi: https://doi.org/10.1007/BF00310770

Boynton, W. V., Taylor, G. J., Evans, L. G., Reedy, R. C., Starr, R., Janes, D. M., ... Hamara, D. K. (2007). Concentration of h, si, cl, k, fe, and th in the low- and mid-latitude regions of mars. *Journal of Geophysical Research*, *112*(E12). doi: https://doi.org/10.1029/2007je002887

Broquet, A., & Andrews-Hanna, J. C. (2022). Geophysical evidence for an active mantle plume underneath Elysium Planitia on Mars. *Nature Astronomy*, 1–10. doi: https://doi.org/10.1038/s41550-022-01836-3

Carr, M. H. (1973). Volcanism on Mars. *J. Geophys. Res.*, *78*, 4049-4062. doi: https://doi.org/10.1029/JB078i020p04049

Christensen, U. (1983). Convection in a variable-viscosity fluid: Newtonian versus power-law rheology. *Earth and Planet. Sci. Lett.*, *64*, 153–162. doi: https://doi.org/10.1016/0012-821X(83)90060-2

Citron, R. I., Manga, M., & Tan, E. (2018). A hybrid origin of the Martian crustal dichotomy: Degree-1 convection antipodal to a giant impact. *Earth and Planet. Sci. Lett.*, *491*, 58-66. doi: https://doi.org/10.1016/j.epsl.2018.03.031

Dannberg, J., & Heister, T. (2016). Compressible magma/mantle dynamics: 3-D, adaptive simulations in ASPECT. *Geophysical Journal International*, *207*(3), 1343–1366. doi: https://doi.org/10.1093/gji/ggw329

Drilleau, M., Samuel, H., Garcia, R. F., Rivoldini, A., Perrin, C., Michaut, C., ... Banerdt, W. B. (2022). Marsquake locations and 1-d seismic models for mars from InSight data. *Journal of Geophysical Research: Planets*, *127*(9). doi: https://doi.org/10.1029/2021je007067

Duncan, M. S., Schmerr, N. C., Bertka, C. M., & Fei, Y. (2018). Extending the solidus for a model iron-rich Martian mantle composition to 25 GPa. *Geophysical Research Letters*, *45*(19), 10,211-10,220. doi: https://doi.org/10.1029/2018GL078182

Elkins-Tanton, L. T. (2005). Possible formation of ancient crust on mars through magma ocean processes. *Journal of Geophysical Research*, *110*(E12). doi: https://doi.org/10.1029/2005je002480

Elkins-Tanton, L. T., Parmentier, E. M., & Hess, P. C. (2003). Magma ocean fractional crystallization and cumulate overturn in terrestrial planets: Implications for Mars. *Meteoritics & Planetary Science*, *38*(12), 1753–1771. doi: https://doi.org/10.1111/j.1945-5100.2003.tb00013.x

Giardini, D., Lognonné, P., Banerdt, W. B., Pike, W. T., Christensen, U., Ceylan, S., ... others (2020). The seismicity of Mars. *Nature Geoscience*, *13*(3), 205–212. doi: https://doi.org/10.1038/s41561-020-0539-8

Hager, B. H., Clayton, R. W., Richards, M. A., Comer, R. P., & Dziewoński, A. M. (1985). Lower mantle heterogeneity, dynamic topography and the geoid. *Nature*, *313*, 541–545.

Harder, H. (1998, July). Phase transitions and the three-dimensional planform of thermal convection in the Martian mantle. *Journal of Geophysical Research: Planets*, *103*(E7), 16775–16797. doi: https://doi.org/10.1029/98je01543

Harder, H. (2000). Mantle convection and the dynamic geoid of Mars. *Geophys. Res. Lett.*, *27*(3), 301-304. doi: https://doi.org/10.1029/2022JE007298

Harer, H., & Christensen, U. R. (1996). A one-plume model of Martian mantle convection. *Nature*, *380*, 507-509.

Hiesinger, H., & Head III, J. W. (2004). The Syrtis Major volcanic province, Mars: Synthesis from Mars global surveyor data. *Journal of Geophysical Research: Planets*, *109*(E1). doi: https://doi.org/10.1029/2003JE002143

Horvath, D. G., Moitra, P., Hamilton, C. W., Craddock, R. A., & Andrews-Hanna, J. C. (2021). Evidence for geologically recent explosive volcanism in Elysium Planitia, Mars. *Icarus*, *365*. doi: https://doi.org/10.1016/j.icarus.2021.114499

Huang, Q., Schmerr, N. C., King, S. D., Kim, D., Rivoldini, A., Plesa, A.-C., ... others (2022). Seismic detection of a deep mantle discontinuity within Mars by InSight. *Proc. Natl. Acad. Sci. U.S.A.*, *119*(42). doi: https://doi.org/10.1073/pnas.2204474119

Hunter, J. D. (2007). Matplotlib: A 2d graphics environment. *Computing in Science & Engineering*, *9*(3), 90–95. doi: https://doi.org/10.1109/MCSE.2007.55

Irving, J. C. E., Lekić, V., Durán, C., Drilleau, M., Kim, D., Rivoldini, A., ... Xu, Z. (2023). First observations of core-transiting seismic phases on Mars. *Proceedings of the National Academy of Sciences*, *120*(18). doi: https://doi.org/10.1073/pnas.2217090120

Jaeger, W. L., Keszthelyi, L. P., Skinner Jr., J. A., Milazzo, M. P., McEwen, A. S., Titus, T. N., ... others (2010). Emplacement of the youngest flood lava on Mars: A short, turbulent story. *Icarus*, *205*(1), 230–243. doi: https://doi.org/10.1016/j.icarus.2009.09.011

Janle, P., & Erkul, E. (1990). Gravity studies of the Tharsis area on Mars. *Earth, Moon, Planets*, *53*, 217-232. doi: https://doi.org/10.1007/BF00055948

Katz, R. F., Spiegelman, M., & Langmuir, C. H. (2003). A new parameterization of hydrous mantle melting. *Geochemistry, Geophysics, Geosystems*, *4*(9). doi: https://doi.org/10.1029/2002GC000433

Khan, A., Ceylan, S., van Driel, M., Giardini, D., Lognonné, P., Samuel, H., ... others (2021). Upper mantle structure of Mars from InSight seismic data. *Science*, *373* (6553), 434–438. doi: https://doi.org/10.1126/science.abf2966

Kiefer, W. S. (2003). Melting in the martian mantle: Shergottite formation and implications for present-day mantle convection on Mars. *Meteorit. Planet. Sci.*, *39* (12), 1815-1832.

Kiefer, W. S. (2008). Forming the martian great divide. *Nature*, *453*, 1191-1192. doi: https://doi.org/10.1038/4531191a

Kiefer, W. S., & Li, Q. (2016). Water undersaturated mantle plume volcanism on present-day Mars. *Meteorit. Planet. Sci.*, *51* (11). doi: https://doi.org/10.1111/maps.12720

Kiefer, W. S., Weller, M. B., Duncan, M. S., & Filiberto, J. (2023, March). Mantle plume magmatism in Elysium Planitia as constrained by InSight seismic observations. In *Lunar and planetary science conference.* The Woodlands, TX, USA.

King, S., & Redmond, H. (2005, March). The crustal dichotomy and edge-driven convection: A mechanism for Tharsis Rise volcanism. In *Lunar and planetary science conference.* The Woodlands, TX, USA. Retrieved from `https://www.lpi.usra.edu/meetings/lpsc2005/pdf/1960.pdf`

King, S. D. (2008). Pattern of lobate scarps on Mercury's surface reproduced by a model of mantle convection. *Nature Geoscience*, *1* (4), 229–232. doi: https://doi.org/10.1038/ngeo152

Knapmeyer-Endrun, B., Panning, M. P., Bissig, F., Joshi, R., Khan, A., Kim, D., … others (2021). Thickness and structure of the martian crust from insight seismic data. *Science*, *373* (6553), 438–443. doi: https://doi.org/10.1126/science.abf8966

Li, Q., & Kiefer, W. S. (2007). Mantle convection and magma production on present-day Mars: Effects of temperature-dependent rheology. *Geophys. Res. Lett.*, *34* (L16203). doi: https://doi.org/10.1029/2007GL030544

Malin, M. C. (1977). Comparison of volcanic features of Elysium (Mars) and Tibesti (Earth). *GSA Bulletin*, *88* (7), 908–919. doi: https://doi.org/10.1130/0016-7606(1977)88⟨908:COVFOE⟩2.0.CO;2

Marinova, M. M., Aharonson, O., & Asphaug, E. (2008). Mega-impact formation of the Mars hemispheric dichotomy. *Nature*, *119*, 1216-1219. doi: https://doi.org/10.1038/nature07070

Matsukage, K. N., Nagayo, Y., Whittaker, M. L., Takahashi, E., & Kawasaki, T. (2013). Melting of the Martian mantle from 1.0 to 4.5 GPa. *Journal of Mineralogical and Petrological Sciences*, *108*, 201–214. doi: https://doi.org/10.2465/jmps.120820

McLennan, S. M. (2001). Crustal heat production and the thermal evolution of mars. *Geophysical Research Letters*, *28* (21), 4019–4022. doi: https://doi.org/10.1029/2001gl013743

Mouginis-Mark, P., Zimbelman, J., Crown, D., Wilson, L., & Gregg, T. (2022). Martian volcanism: Current state of knowledge and known unknowns. *Geochemistry*, *82*. doi: https://doi.org/10.1016/j.chemer.2022.125886

Neukum, G., Jaumann, R., Hoffmann, H., Hauber, E., Head, J., A.T., B., … the HRSC Investigator Team (2004). Recent and episodic volcanic and glacial activity on Mars revealed by the High Resolution Stereo Camera. *Nature*, *432*, 971-979. doi: https://doi.org/10.1038/nature03231

Neumann, G., Zuber, M., Wieczorek, M., McGovern, P., Lemoine, F., & Smith, D. (2004). Crustal structure of Mars from gravity and topography. *J. Geophys. Res.*, *109* (E08002). doi: https://doi.org/10.1029/2004JE002262

Perrin, C., Jacob, A., Lucas, A., Myhill, R., Hauber, E., Batov, A., … Fuji, N. (2022). Geometry and Segmentation of Cerberus Fossae, Mars: Implications for Marsquake Properties. *Journal of Geophysical Research: Planets*, *127* (1). doi: https://doi.org/10.1029/2021je007118

Phillips, R., Zuber, M., Solomon, S., Golombek, M., Jakosky, B., Banerdt, W., …

Hauck II, S. (2001). Ancient geodynamics and global-scale hydrology on Mars. *Science*, *291*, 2587-2591. doi: https://doi.org/10.1126/science.1058701

Platz, T., Michael, G. G., & Neukum, G. (2010). Confident thickness estimates for planetary surface deposits from concealed crater populations. *Earth and Planet. Sci. Lett.*, *293*, 388–395. doi: https://doi.org/10.1016/j.epsl.2010.03.012

Plesa, A.-C., Grott, M., Tosi, N., Breuer, D., Spohn, T., & Wieczorek, M. (2016). How large are present-day heat flux variations across the surface of Mars? *J. Gephys. Res. Planets*, *121*, 2386-2403. doi: https://doi:10.1002/2016JE005126

Plesa, A.-C., Knapmeyer, M., Golombek, M., Breuer, D., Grott, M., Kawamura, T., ... Weber, R. (2018). Present-day Mars' seismicity predicted From 3-D thermal evolution models of interior dynamics. *Geophys. Res. Lett.*, *45*, 2580-2589. doi: https://doi.org/10.1002/2017GL076124

Plesa, A.-C., Tosi, N., Grott, M., & Breuer, D. (2015). Thermal evolution and Urey ratio of Mars. *J. Gephys. Res. Planets*, *120*, 995-1010. doi: https://doi.org/10.1002/2014JE004748

Richardson, J., Wilson, J., Connor, C., Bleacher, J., & Kiyosugi, K. (2017). Recurrence rate and magma effusion rate for the latest volcanism on Arsia Mons, Mars. *Earth Planet. Sci. Lett.*, *458*, 170-178. doi: https://doi.org/10.1016/j.epsl.2016.10.040

Roberts, J. H., & Zhong, S. (2004). Plume-induced topography and geoid anomalies and their implications for the Tharsis rise on Mars. *J. Geophys. Res. Planets*, *109*(E03009). doi: https://doi.org/10.1029/2003JE002226

Roberts, J. H., & Zhong, S. (2006). Degree-1 convection in the Martian mantle and the origin of the hemispheric dichotomy. *J. Geophys. Res. Planets*, *111*(E06013). doi: https://doi.org/10.1029/2005JE002668

Ruedas, T., Tackley, P. J., & Solomon, S. C. (2013). Thermal and compositional evolution of the martian mantle: Effects of water. *Physics of the Earth and Planetary Interiors*, *220*, 50-72. doi: https://doi.org/10.1016/j.pepi.2013.04.006

Samuel, H., Ballmer, M. D., Padovan, S., Tosi, N., Rivoldini, A., & Plesa, A.-C. (2021). The thermo-chemical evolution of Mars with a strongly stratified mantle. *J. Geophys. Res. Planets*, *126*. doi: https://doi.org/10.1029/2020JE006613

Sekhar, P., & King, S. D. (2014). 3D spherical models of Martian mantle convection constrained by melting history. *Earth Planet. Sci. Lett.*, *388*, 27–37. doi: https://doi.org/10.1016/j.epsl.2013.11.047

Smrekar, S. E., Lognonné, P., Spohn, T., Banerdt, W. B., Breuer, D., et al. (2019). Pre-mission InSights on the Interior of Mars. *Space Science Reviews*, *215*(1), 1–72. doi: https://doi.org/10.1007/s11214-018-0563-9

Šrámek, O., & Zhong, S. (2012). Martian crustal dichotomy and Tharsis formation by partial melting coupled to early plume migration. *Journal of Geophysical Research: Planets*, *117*(E1). doi: https://doi.org/10.1029/2011JE003867

Stähler, S. C., Khan, A., Banerdt, W. B., Lognonné, P., Giardini, D., Ceylan, S., ... others (2021). Seismic detection of the martian core. *Science*, *373*(6553), 443–448. doi: https://doi.org/10.1126/science.abi7730

Stähler, S. C., Mittelholz, A., Perrin, C., Kawamura, T., Kim, D., Knapmeyer, M., ... others (2022). Tectonics of Cerberus Fossae unveiled by marsquakes. *Nature Astronomy*, *6*(12), 1376–1386. doi: https://doi.org/10.1038/s41550-022-01803-y

Stähler, S. C., Mittelholz, A., Perrin, C., Kawamura, T., Kim, D., Knapmeyer, M., ... Banerdt, W. B. (2022). Tectonics of Cerberus Fossae unveiled by marsquakes. *Nature Astronomy*, *6*(12), 1376–1386. doi: https://doi.org/10.1038/s41550-022-01803-y

Stevenson, D. J., Spohn, T., & Schubert, G. (1983). Magnetism and thermal evolution of the terrestrial planets. *Icarus*, *54*(3), 466–489. doi: https://doi.org/10.1016/0019-1035(83)90241-5

Susko, D., Karunatillake, S., Kodikara, G., Skok, J. R., Wray, J., Heldmann, J., . . . Judice, T. (2017). A record of igneous evolution in Elysium, a major martian volcanic province. *Scientific Reports*, *7*(1). doi: https://doi.org/10.1038/srep43177

Tan, E., Choi, E., Thoutireddy, P., Gurnis, M., & Aivazis, M. (2006). GeoFramework: Coupling multiple models of mantle convection within a computational framework. *Geochem. Geophys. Geosyst.*, *7*(Q06001). doi: https://doi.org/10.1029/2005GC001155

Taylor, G. J., Boynton, W., Brückner, J., Wänke, H., Dreibus, G., Kerry, K., . . . Drake, D. (2006). Bulk composition and early differentiation of mars. *Journal of Geophysical Research*, *112*(E3). doi: https://doi.org/10.1029/2005je002645

Tosi, N., Plesa, A.-C., & Breuer, D. (2013). Overturn and evolution of a crystallized magma ocean: A numerical parameter study for Mars. *J. Geophys. Res. Planets*, *118*, 1512-1528. doi: https://doi.org/10.1002/jgre.20109

Turcotte, D. L., & Schubert, G. (2014). *Geodynamics*. Cambridge, UK: Cambridge University Press. doi: https://doi.org/10.1017/CBO9780511843877

Šrámek, O., & Zhong, S. (2012). Martian crustal dichotomy and Tharsis formation by partial melting coupled to early plume migration. *J. Geophys. Res.*, *117*(E01005). doi: https://doi.org/10.1029/2011JE003867

van Thienen, P., Rivoldini, A., Van Hoolst, T., & Lognonné, P. (2006). A top-down origin for martian mantle plumes. *Icarus*. doi: https://doi:10.1016/j.icarus.2006.06.008.

Vaucher, J., Baratoux, D., Mangold, N., Pinet, P., Kurita, K., & Grégoire, M. (2009). The volcanic history of central Elysium Planitia: Implications for martian magmatism. *Icarus*, *204*(2), 418–442. doi: https://doi.org/10.1016/j.icarus.2009.06.032

Wänke, H., & Dreibus, G. (1994). Chemistry and accretion history of mars. *Philosophical Transactions of the Royal Society of London. Series A: Physical and Engineering Sciences*, *349*(1690), 285–293.

Watson, S., & McKenzie, D. (1991). Melt generation by plumes: a study of Hawaiian volcanism. *Journal of Petrology*, *32*(3), 501–537. doi: https://doi.org/10.1093/petrology/32.3.501

Watters, T., & Schubert, G. (2007). Hemispheres apart: The crustal dichotomy on Mars. *Annu. Rev. Earth Planet. Sci.*, *35*, 621-652. doi: https://doi:10.1146/annurev.earth.35.031306.140220

Wenzel, M. J., Manga, M., & Jellinek, A. M. (2004). Tharsis as a consequence of Mars' dichotomy and layered mantle. *Geophys. Res. Lett.*, *31*(L04702). doi: https://doi.org/10.1029/2003GL019306

Wieczorek, M. A., Broquet, A., McLennan, S. M., Rivoldini, A., Golombek, M., Antonangeli, D., . . . others (2022). InSight constraints on the global character of the Martian crust. *J. Geophys. Res. Planets*, *127*. doi: https://doi.org/10.1029/2022JE007298

Wieczorek, M. A., & Meschede, M. (2018, August). SHTools: Tools for working with spherical harmonics. *Geochemistry, Geophysics, Geosystems*, *19*(8), 2574–2592. doi: https://doi.org/10.1029/2018gc007529

Zhong, S. (2009). Migration of Tharsis volcanism on Mars caused by differential rotation of the lithosphere. *Nature Geoscience*, *2*, 19-23. doi: https://doi.org/10.1038/NGEO392

Zhong, S., McNamara, A., Tan, E., Moresi, L., & Gurnis, M. (2008). A benchmark study on mantle convection in a 3-D spherical shell using CitcomS. *Geochem. Geophys. Geosyst.*, *9*(10). doi: https://doi.org/10.1029/2008GC002048

Zhong, S., Zuber, M. T., Moresi, L., & Gurnis, M. (2000). Role of temperature-dependent viscosity and surface plates in spherical shell models of mantle convection. *J. Geophys. Res.*, *105*(B5), 11,063-11,082. doi: https://doi.org/10.1111/maps.12720

Zuber, M., & Smith, D. (1997). Mars without Tharsis. *J. Geophys. Res.*, *102*(E12), 28,673-28,685. doi: https://doi.org/10.1029/97JE02527

Zuber, M., Solomon, S., Phillips, R., Smith, D., Tyler, G., Aharonson, O., … Zhong, S. (2000). Internal structure and early thermal evolution of Mars from Mars Global Surveyor topography and gravity. *Science*, *287*(1788). doi: https://doi.org/10.1126/science.287.5459.1788

Tables

Table 1: Summary of parameters and initial conditions used in our models.

Parameter	Value
Mean radius	3.3895×10^{6} m
Core radius	1.830×10^{6} m
Mean mantle density	$3500\,\mathrm{kg\,m^{-3}}$
Gravitational acceleration (g)	$3.72\,\mathrm{m\,s^{-2}}$
Reference viscosity (η_0)	1.0×10^{21} Pa s
Activation energy (E*)	$117\,\mathrm{kJ\,mol^{-1}}$ (low)
	$350\,\mathrm{kJ\,mol^{-1}}$ (high)
Activation volume (V*)	$6.6\,\mathrm{cm^3\,mol^{-1}}$
Rayleigh number (Ra), mantle thickness[a]	1.4296×10^{7}
Thermal expansivity (α)	$2 \times 10^{-5}\,\mathrm{K^{-1}}$
Thermal diffusivity (κ)	$1 \times 10^{-6}\,\mathrm{m^2\,s^{-1}}$
Specific heat capacity (c_P)	$1.25 \times 10^{3}\,\mathrm{J\,kg^{-1}\,K^{-1}}$
Mantle adiabat	$0.15\,\mathrm{K\,km^{-1}}$
Surface Temperature (T_s)	220 K
Temperature difference (ΔT)	1500 K
Initial mantle temperature[b]	1720 K
Initial CMB temperature[b]	1720 K (1.0 ΔT)
	1870 K (1.1 ΔT)
	2020 K (1.2 ΔT)
Crustal HPE enrichment factor	5x
	10x
	15x
Present-day bulk ^{238}U	15.88 ppm [c]
Present-day bulk ^{235}U	0.11 ppm [c]
Present-day bulk ^{232}Th	56.0 ppm [c]
Present-day bulk K	305 ppm [c]
Present-day bulk ^{40}K	36.3 ppm [c]

[a] Rescaled from model because CitcomS uses radius instead of mantle thickness for its Ra
[b] Potential temperature: excludes adiabat
[c] Present-day bulk silicate Mars HPE concentrations from Wänke and Dreibus (1994)

Table 2: Quantitative comparison of our model geoids (model) to that of Mars without Tharsis (MWT) (Zuber & Smith, 1997) for degrees ℓ=2–6.

Rheology	Enrichment	T_{CMB}	NRMSE[a]
Uniform, low E*	5x	1720 K	0.9877
Uniform, low E*	5x	1870 K	0.9693
Uniform, low E*	5x	2020 K	0.9601
Uniform, low E*	10x	1720 K	0.8245
Uniform, low E*	10x	1870 K	0.7820
Uniform, low E*	10x	2020 K	0.7619
Uniform, low E*	15x	1720 K	0.3918
Uniform, low E*	15x	1870 K	0.2046
Uniform, low E*	15x	2020 K	0.5368
Uniform, high E*	5x	1720 K	0.8826
Uniform, high E*	5x	1870 K	0.7702
Uniform, high E*	5x	2020 K	0.4637
Uniform, high E*	10x	1720 K	0.4260
Uniform, high E*	10x	1870 K	0.5013
Uniform, high E*	10x	2020 K	0.4892
Uniform, high E*	15x	1720 K	2.185
Uniform, high E*	15x	1870 K	1.635
Uniform, high E*	15x	2020 K	1.128
Dichotomy, high E*	5x	1720 K	0.9459
Dichotomy, high E*	5x	1870 K	0.8921
Dichotomy, high E*	5x	2020 K	0.7433
Dichotomy, high E*	10x	1720 K	0.8787
Dichotomy, high E*	10x	1870 K	0.8516
Dichotomy, high E*	10x	2020 K	0.3955
Dichotomy, high E*	15x	1720 K	0.7161
Dichotomy, high E*	15x	1870 K	0.5515
Dichotomy, high E*	15x	2020 K	1.978

[a] See text.

Table 3: Model time and age of last melt production

Rheology[a]	Enrichment	T_{CMB}	Model time	Age BP[b,c]
Uniform, low E*	5x	1720 K	4500 Myr	0 Ma
Uniform, low E*	5x	1870 K	4483 Myr	17 Ma
Uniform, low E*	5x	2020 K	4500 Myr	0 Ma
Uniform, low E*	10x	1720 K	3154 Myr	1346 Ma
Uniform, low E*	10x	1870 K	3615 Myr	884 Ma
Uniform, low E*	10x	2020 K	4142 Myr	358 Ma
Uniform, low E*	15x	1720 K	2105 Myr	2395 Ma
Uniform, low E*	15x	1870 K	3129 Myr	1371 Ma
Uniform, low E*	15x	2020 K	2560 Myr	1940 Ma
Uniform, high E*	5x	1720 K	4500 Myr	0 Ma
Uniform, high E*	5x	1870 K	4500 Myr	0 Ma
Uniform, high E*	5x	2020 K	4500 Myr	0 Ma
Uniform, high E*	10x	1720 K	3756 Myr	744 Ma
Uniform, high E*	10x	1870 K	4500 Myr	0 Ma
Uniform, high E*	10x	2020 K	4354 Myr	146 Ma
Uniform, high E*	15x	1720 K	2080 Myr	2420 Ma
Uniform, high E*	15x	1870 K	3785 Myr	715 Ma
Uniform, high E*	15x	2020 K	4229 Myr	271 Ma
Dichotomy, high E*	5x	1720 K	4100 Myr	0 Ma
Dichotomy, high E*	5x	1870 K	4100 Myr	0 Ma
Dichotomy, high E*	5x	2020 K	4100 Myr	0 Ma
Dichotomy, high E*	10x	1720 K	4100 Myr	0 Ma
Dichotomy, high E*	10x	1870 K	4100 Myr	0 Ma
Dichotomy, high E*	10x	2020 K	4100 Myr	0 Ma
Dichotomy, high E*	15x	1720 K	3028 Myr	1072 Ma
Dichotomy, high E*	15x	1870 K	3210 Myr	890 Ma
Dichotomy, high E*	15x	2020 K	4100 Myr	0 Ma

[a] E* is activation energy.
[b] Uniform cases are taken to start at 4.5 Ga.
[c] Dichotomy cases are taken start 400 Myr later, at 4.1 Ga.

967 # Figures

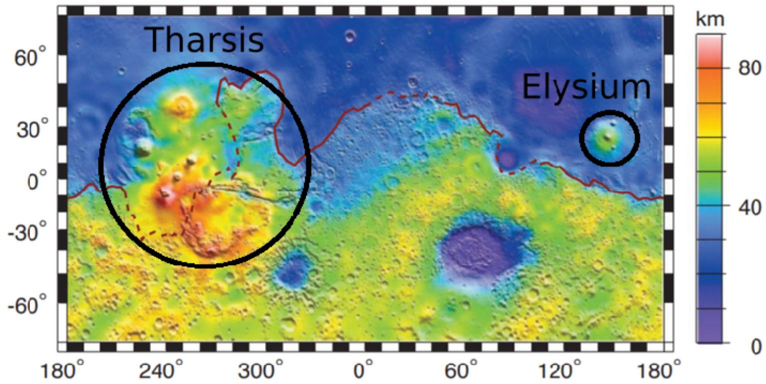

Figure 1: Crustal thickness map adapted from Zuber et al. (2000). The locations and approximate extent of Tharsis and Elysium are marked. The red line marks the dichotomy boundary. The line is dashed where the boundary is uncertain, in particular beneath Tharsis.

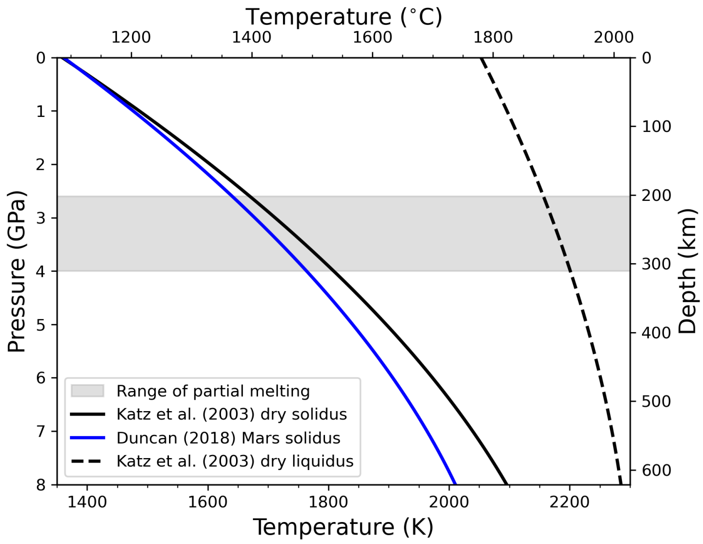

Figure 2: Comparison of the Katz et al. (2003) solidus for dry peridotite with the Mars solidus of Duncan et al. (2018) over the applicable depth range of Katz et al. (2003). The liquidus of Katz et al. (2003) is also plotted. Melting in our models is confined to a narrow range of pressures between 2.6 and 4 GPa, or approximately 200–300 km depth.

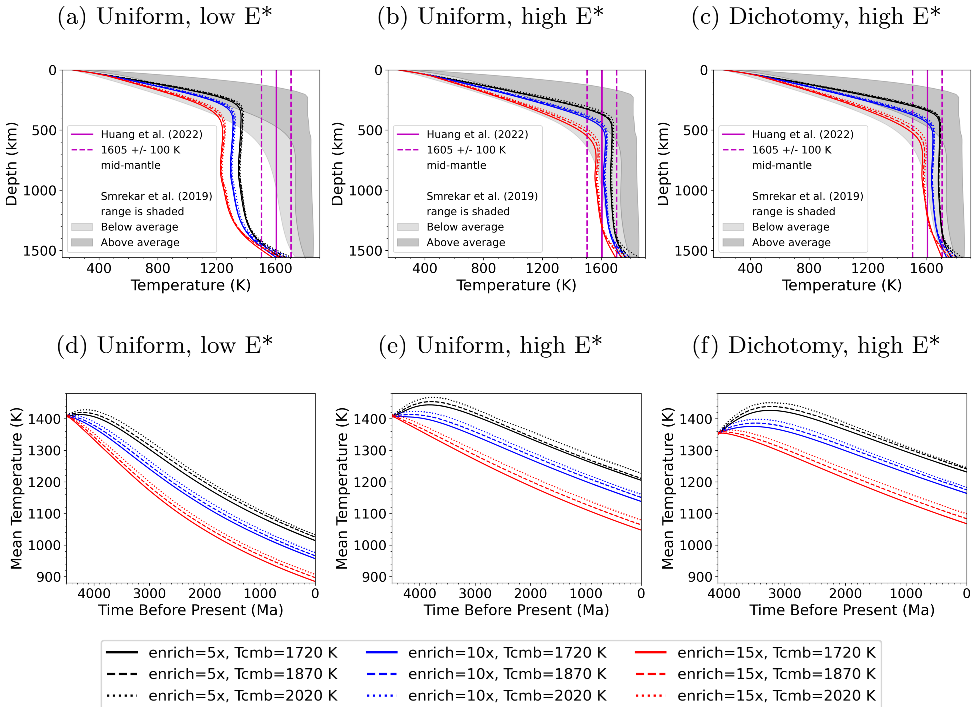

Figure 3: (a–c): Present-day geotherms, including the InSight derived mid-mantle temperature estimate of 1605±100 K by Huang et al. (2022) (vertical magenta lines), as well as the range of possible geotherms from Smrekar et al. (2019) (shaded). (d–e): Mean mantle temperature vs. time. E* is activation energy.

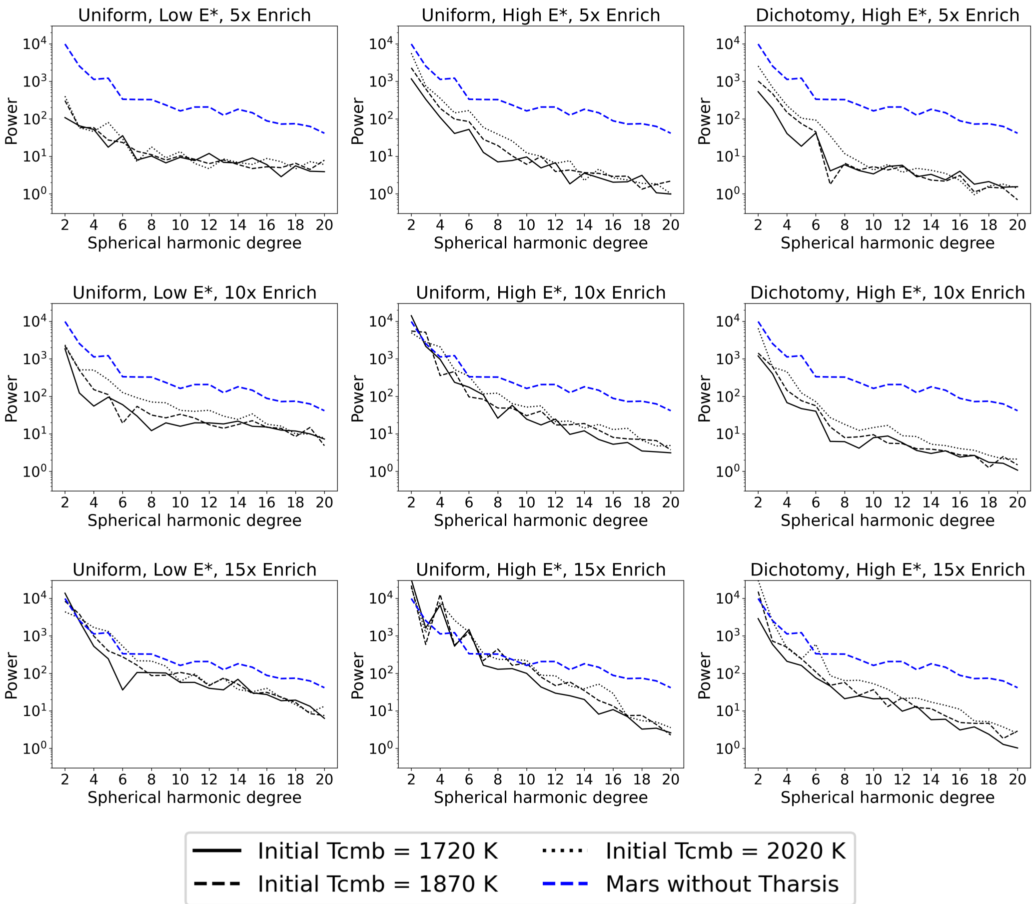

Figure 4: Power spectra (degrees ℓ=2–20) of our modeled present-day geoids (black) compared to the Mars without Tharsis (blue dashed) geoid derived from the gravity coefficients of Zuber and Smith (1997).

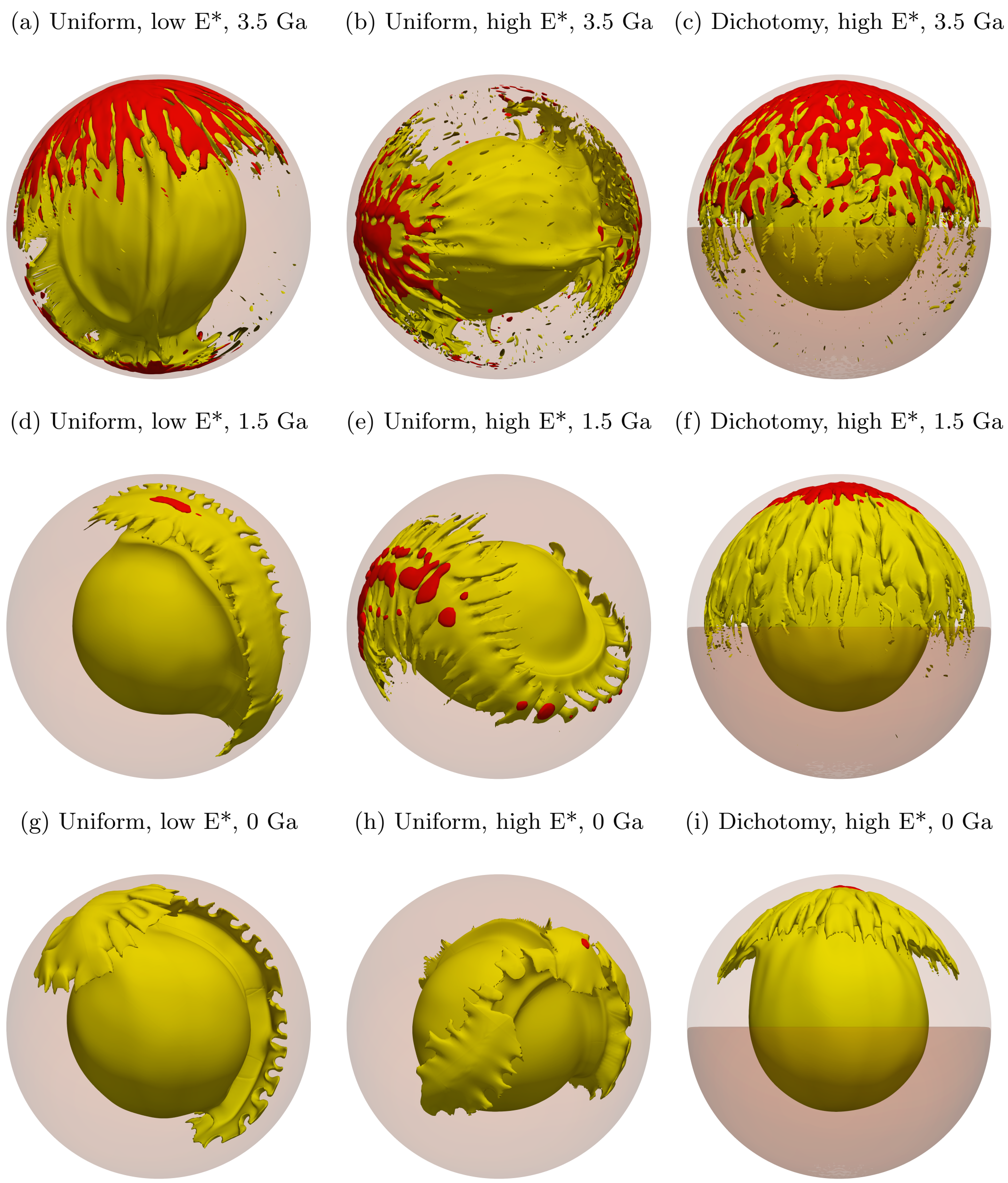

Figure 5: 3D plots of selected model cases with potential temperature isotherms (yellow) and melt (red) for all three (uniform, low activation energy; uniform, high activation energy; dichotomy, high activation energy) cases with 10x enrichment and initial T_{CMB} of 1870 K. The temperature and melt abundance vary widely both between the model cases and through time. Therefore, the plotted isotherms and melt thresholds for each model and time step are selected to be representative of the thermal structure and the highest melt concentration in the specified model at the specified time. The values chosen are as follows: (a) T = 1650 K, melt fraction $\geq$ 10%; (b) T = 1770 K, melt fraction $\geq$ 25%; (c) T = 1755 K, melt fraction $\geq$ 25%; (d) T = 1500 K, melt fraction $\geq$ 0.01%; (e) T = 1710 K, melt fraction $\geq$ 0.1%; (f) T = 1710 K, melt fraction $\geq$ 1%; (g) T = 1380 K, no melt present; (h) T = 1680 K, melt fraction $\geq$ 0.01%; and (i) T = 1680 K, melt fraction $\geq$ 1%. The southern hemisphere, with the initially thicker lithosphere, is darker in all dichotomy plots (c, f, i). For the remaining plots, north is approximately up, but some rotation has been done to better show the structure and melt.

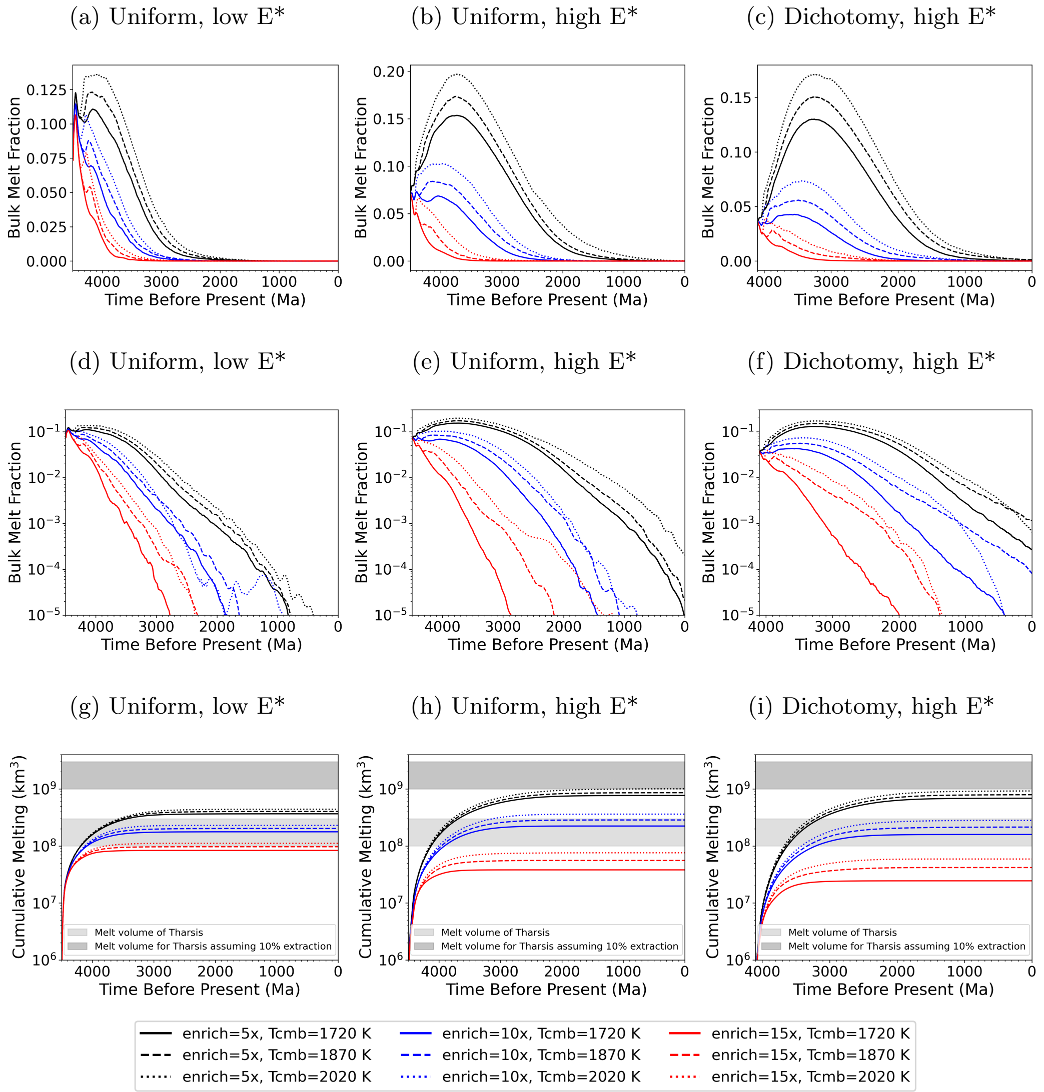

Figure 6: Melt and melt production over time. The bulk melt fraction is the fraction of the total mantle (out of 1.0) that is molten at a given time. This is shown here both on a linear and logarithmic scale. Cumulative melt is the integral of the mantle melt production rate over time. On the cumulative melt plots (g–i), the approximate amount of melt (1–3 $\times 10^8$ km^3) required to produce Tharsis is shaded in lighter gray. However, only a fraction of the melt (here assumed to be 10%) produced in the mantle is extracted to and erupted on the surface. The darker gray shading on these same plots is the required melt volume multiplied by ten (1–3 $\times 10^9$ km^3) to account for this.

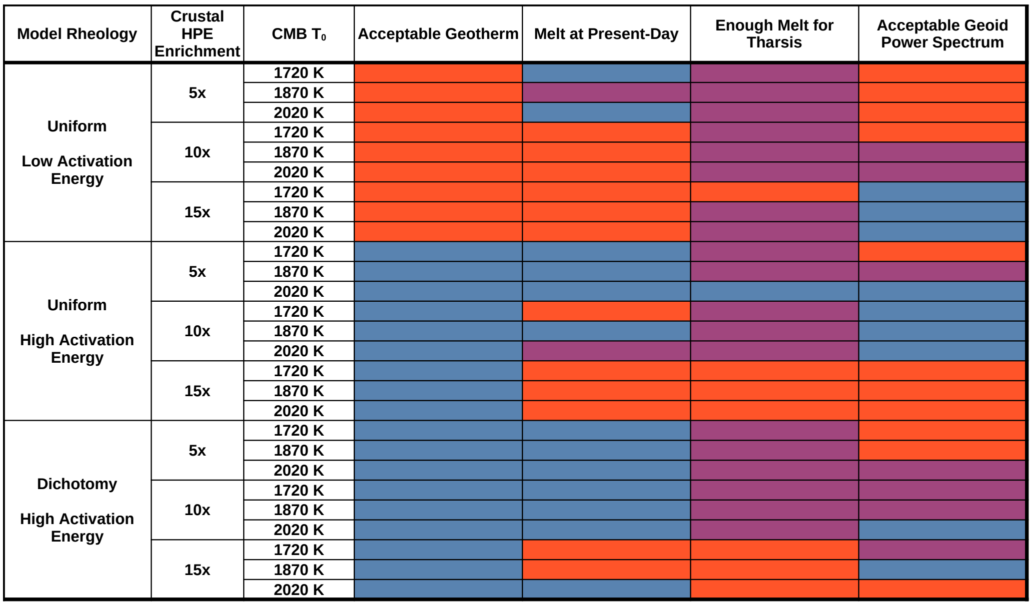

Figure 7: Blue indicates the constraint is met, and red that it is not. Purple indicates an intermediate result (geoids) or that the constraint is met with qualification. See discussion text for the quantitative meaning of these colors for each column.

Reconciling Mars InSight Results, Geoid, and Melt Evolution with 3D Spherical Models of Convection

J. P. Murphy[1], S. D. King[1]

[1]Virginia Polytechnic Institute and State University
[1]Blacksburg, VA, USA

Key Points:

- Our results favor a higher activation energy mantle rheology and 10x crustal heat producing element enrichment factor
- It is not difficult to produce melt up to the present-day, even with a cool mantle consistent with InSight results
- It is very difficult to produce sufficient melt for Tharsis without assuming extremely efficient extraction of mantle melt to the surface

Corresponding author: Josh Murphy, `jmurph16@vt.edu`

Abstract

We investigate the geodynamic and melting history of Mars using 3D spherical shell models of mantle convection, constrained by the recent InSight mission results. The Martian mantle must have produced sufficient melt to emplace the Tharsis rise by the end of the Noachian–requiring on the order of 1–3$\times10^9$ km^3 of melt after accounting for limited ($\sim$10%) melt extraction. Thereafter, melting declined, but abundant evidence for limited geologically recent volcanism necessitates some melt even in the cool present-day mantle inferred from InSight data. We test models with two mantle activation energies, and a range of crustal Heat Producing Element (HPE) enrichment factors and initial core-mantle boundary temperatures. We also test the effect of including a hemispheric (spherical harmonic degree-1) step in lithospheric thickness to model the Martian dichotomy. We find that a higher activation energy ($350\,\mathrm{kJ\,mol^{-1}}$) rheology produces present-day geotherms consistent with InSight results, and of those the cases with HPE enrichment factors of 5–10x produce localized melting near or up to present-day. 10x crustal enrichment is consistent with both InSight and geochemical results, and those models also produce present-day geoid power spectra consistent with Mars. However, it is very difficult to produce sufficient melt to form Tharsis in a mantle that also matches the present-day geotherm, without assuming extremely efficient extraction of melt to the surface. The addition of a degree-1 hemispheric dichotomy, as an equatorial step in lithospheric thickness, does not significantly improve upon melt production or the geoid.

Plain Language Summary

Mars' mantle needed to produce an extremely high volume of melt by $\sim$3.7 billion years ago in order to build the immense volcanic plateau of Tharsis. There is also significant evidence for small volumes of geologically recent volcanism, yet InSight mission results indicate relatively cool mantle at present. We use 3D numerical models of the Martian mantle to determine what properties can produce a melting history and present interior temperatures consistent with InSight results and Mars' volcanic history. We test sets of models with two different mantle activation energies (how sensitive the mantle viscosity is to changes in temperature), and a range of crustal Heat Producing Element enrichment factors. We also test the effect of including a simplified version of the Martian hemispheric dichotomy. Our models with the higher activation energy and 10x crustal enrichment (consistent with Mars' crustal composition) produce melt near the present-day as well as temperature profiles consistent with InSight. However, it is very difficult to produce sufficient melt to form Tharsis in such a cool mantle, without assuming most of the melt produced in the mantle reaches the surface. Addition the simplified dichotomy does not significantly improve our results.

1 Introduction

Results from the InSight mission provide new constraints on the temperature, structure, and geodynamic evolution of the Martian interior. The InSight mission was the first to record quakes (unambiguously) and impacts on Mars (Banerdt et al., 2020; Giardini et al., 2020). Using reflections of seismic waves from the core-mantle boundary of Mars together with geodetic data, Stähler et al. (2021) constrained the radius of the liquid metal core to be 1830$\pm$40 km with a mean core density of 5700–6300 kg/m^3–implying that there is 10–15 wt. % S in addition to other light elements dissolved in the nickle-iron core. The core radius is at the large end of the pre-mission estimate (Smrekar et al., 2019) and, implies that there is no bridgmanite layer above the core-mantle boundary. The absence of a bridgmanite layer is an important constraint for mantle dynamics because a thin bridgmanite layer is one mechanism to generate degree-1 convection (Harer & Christensen, 1996; Harder, 1998, 2000).

The topography and crustal thickness of Mars are characterized by the dichotomy between the northern and southern hemispheres. The northern hemisphere is dominated by lowlands which tend to have thinner crust, while the southern hemisphere is dominated by heavily cratered highlands which tend to have a thicker crust. Using InSight seismic data, Knapmeyer-Endrun et al. (2021) found two possible Moho depths, the first at 20±5 km and the second at 39±8 km. The thicker crust is more consistent with the surface composition, while the thinner crust would require an increasing HPE concentration with depth. The thicker crust would also allow a slightly higher bulk crustal density ($3100\,\mathrm{kg\,m^{-3}}$) when compared with the thinner crust ($<2900\,\mathrm{kg\,m^{-3}}$). Considering either model and the aforementioned gravity and topography data sets, Wieczorek et al. (2022) constrain the global average Martian crustal thickness to be between 24 and 72 km, with thinner crust in the lowlands (including the InSight landing site), and thicker crust beneath the highlands and Tharsis.

Huang et al. (2022) constrained the depth of a mid-mantle discontinuity to be 1,006±40 km by modeling triplicated P and S waveforms. Interpreting this seismic discontinuity as the transformation of olivine to a higher-pressure polymorph (likely ringwoodite) yields a mantle potential temperature of 1,605±100 K. Using a parameterized convection approach, Huang et al. (2022) suggest that the mantle potential temperature was 1,720 to 1,860 K soon after formation. When combining the 1,000-depth phase transition transition with an estimated crustal thickness from Knapmeyer-Endrun et al. (2021), a present-day lithospheric thickness of 400-600 km (Khan et al., 2021), and moment of inertia and love number constraints, Huang et al. (2022) prefer a model with 10 to 15x crustal HPE enrichment and present-day average surface heat flow of 21 to 24 mW/m^2, implying a relatively sluggish mantle with a reference viscosity of 10^{20}–10^{22} Pa s. The InSight-constrained geodynamic modeling of Samuel et al. (2021) favor 10x crustal enrichment, and orbital gamma ray spectrometry also supports an enrichment of ∼10-15x (Boynton et al., 2007; McLennan, 2001; Taylor et al., 2006).

In addition to the new results from InSight, geodynamic models must also be consistent with the observed volcanic history of Mars. Mars' volcanic history, as well as the present-day topography and gravity field, are dominated by the Tharsis rise, a broad dome 8000 km in diameter and 10 km high–far larger than any terrestrial igneous province–containing several large volcanoes, centered in the equatorial western hemisphere (Janle & Erkul, 1990). The origin of the Tharsis rise is generally ascribed to one or more long-lived mantle plumes (Carr, 1973; Harer & Christensen, 1996; Kiefer, 2003; Li & Kiefer, 2007). While most of the rise itself was emplaced by lava lows by the end of the Noachian, and the large volcanic shields in the Hesperian, the region has remained volcanically active for most of the planet's history (Phillips et al., 2001; Neukum et al., 2004; Richardson et al., 2017). According to Neukum et al. (2004), there is evidence of volcanism in Tharsis as recently as 2.4 million years ago. The relatively recent volcanic and tectonic activity, and modeled long-term stability of convection in the Martian mantle indicates that mantle melting is still occurring in the present day (Kiefer, 2003; Li & Kiefer, 2007; Kiefer & Li, 2016).

The Tharsis rise straddles the boundary between the thicker crust of the southern highlands and the thinner crust of the northern lowlands (Neumann et al., 2004). The contrast between these two hemispheres (zonal degree-1 topography) is referred to as the Martian crustal dichotomy. This feature is apparent in the hypsometry (elevation frequency distribution) of Mars, which has a bimodal distribution with peaks separated by 5.5 km (Aharonson et al., 2001; Watters & Schubert, 2007). The origin of the dichotomy is still highly uncertain. It may be of internal origin, for example the result of degree-1 mantle convection (Roberts & Zhong, 2006; Zhong, 2009), or from a giant impact (Andrews-Hanna et al., 2008; Kiefer, 2008; Marinova et al., 2008). A hybrid origin from degree-1 mantle convection caused by the giant impact has also been proposed (Citron et al., 2018). Several studies have considered a causal link between the dichotomy and Tharsis (S. King & Redmond, 2005; Šrámek & Zhong, 2012; van Thienen et al., 2006; Wenzel et al., 2004; Zhong, 2009). S. King and Redmond (2005) propose that Tharsis is the result of small-scale convection at the dichotomy boundary caused by the difference in crustal or lithospheric thickness.

However, there are other significant volcanic regions besides Tharsis, including the Elysium rise which is a smaller version of Tharsis but, still comparable in size to the largest igneous provinces on Earth. Unlike Tharsis, the Elysium rise itself and its volcanic shields appear to have had less recent volcanic activity than Olympus Mons and the Tharsis Montes associated with Tharsis swell, with a steep decline after a peak $\sim$1 Ga (Platz et al., 2010; Susko et al., 2017). However, the greater Elysium region shows evidence of more recent activity to the southeast of the rise, including volcanism within the past 0.2-20 Myr in Elysium Planitia, and in particular Cerberus Fossae (Susko et al., 2017; Horvath et al., 2021; Berman & Hartmann, 2002; Vaucher et al., 2009; Jaeger et al., 2010). Geophysical evidence also supports recent and presently active tectonism, possibly driven by magma, in Cerberus Fossae, as well a possibly active mantle plume beneath Elysium Planitia (Stähler et al., 2022; Broquet & Andrews-Hanna, 2022). Between Tharsis and Elysium lies the vast lava plain of Amazonis Planitia, produced by lava flows of the late, eponymous, Amazonian Period. Other, much older, volcanic regions of significance include the Syrtis Major province, as well parts of the Southern Highlands such as Tyrrhenus Mons and Hadriacus Mons (Hiesinger & Head III, 2004; Mouginis-Mark et al., 2022).

Geoid anomalies provide another constraint on the dynamics of planetary interiors (Hager et al., 1985; Roberts & Zhong, 2004; S. D. King, 2008). However, as Mars' gravity field and geoid are dominated by the topography of the Tharsis rise, largely built up by lava flows, removing or greatly reducing the effect of Tharsis from Mars' measured gravity field allows a much more useful comparison with our model geoids. Zuber and Smith (1997) calculated the low-degree (ℓ=2-6) coefficients for Mars without Tharsis (MWT), which we use for comparison–though this MWT geoid retains shorter wavelength features associated with Elysium, as well the large shields of Tharsis, as well as large impact basins such as Utopia and Hellas. (Spherical shell modeling does not include or produce the topography built up by lava or excavated by impacts.)

Using the 3D spherical shell geodynamic code CitcomS (Zhong et al., 2000; Tan et al., 2006; Zhong et al., 2008), we investigate the thermal and volcanic history of Mars. We consider runs successful if they are capable of producing: present-day temperature profiles (geotherms or potential temperatures) that fall within the range inferred from InSight results (Khan et al., 2021; Huang et al., 2022); geoid and topography power spectra consistent the the observations after removing the effect of Tharsis (Zuber & Smith, 1997), and sufficient melt in the first billion years to explain the widespread volcanism with isolated pockets of melt at present day. If the models are too hot, they will produce a persistent global melt layer lasting billions of years, while if they cool too quickly, melt production will be too low and end too early to be consistent with Mars. The observation of volcanic activity within the past 100 million, and even past few million years (Berman & Hartmann, 2002; Horvath et al., 2021; Jaeger et al., 2010; Neukum et al., 2004; Vaucher et al., 2009), means that acceptable models should produce small amounts of melt up to, or at least near, present-day.

Elysium is comparable in size to the largest terrestrial igneous provinces. Like Tharsis it also comprises a broad rise (2400 km $\times$ 1700 km) topped by large volcanoes and shows evidence for billions of years of volcanic activity–albeit not as recently as Tharsis, with a steep decline in volcanism after a peak $\sim$1 Ga (Malin, 1977; Platz et al., 2010; Susko et al., 2017). However, the greater Elysium region shows evidence of more recent activity to the south and southeast of the rise, including volcanism within the past 0.2-20 Myr in Elysium Planitia (the region where InSight landed), and in particular Cerberus Fossae (Susko et al., 2017; Horvath et al., 2021; Berman & Hartmann, 2002; Vaucher et al., 2009; Jaeger et al., 2010). Geodynamicists have typically focused on Tharsis, because Elysium and its three major volcanoes, while large by Earth standards, are markedly smaller than Tharsis and its largest volcanoes. Therefore, Martian volcanism has been modeled as a single long-lived plume (Harer & Christensen, 1996). The mantle convective structure in this one-plume model is represented by a sectoral degree-1 spherical harmonic, where the hemisphere containing Tharsis is dominated by upwelling from the plume and the other hemisphere is dominated by downwelling (Roberts & Zhong, 2006). Others, including Kiefer (2003); Li and Kiefer (2007); Kiefer and Li (2016), favor a multi-plume model for Tharsis. Instead of one very large plume, there would be a group of smaller plumes under Tharsis, each feeding one of the main volcanoes. Such plumes have been modeled as stable over billions of years and ongoing melt production at their centers would explain the continued volcanic activity over this time period, even to the present-day Li and Kiefer (2007).

2 Methods

2.1 CitcomS

We model the Martian mantle using a modified version of the finite element geodynamics code CitcomS (Zhong et al., 2000; Tan et al., 2006; Zhong et al., 2008). The solid mantle behaves as an extremely viscous fluid over long timescales, which is modeled as a creeping flow. CitcomS solves the following nondimensionalized equations for the conservation of mass, momentum, and energy, respectively:

$$\nabla \cdot \mathbf{u} = 0 \tag{1}$$

$$-\nabla P + \nabla \cdot \left[\eta \left(\nabla \mathbf{u} + \nabla^T \mathbf{u}\right)\right] + RaT\mathbf{e}_r = 0 \tag{2}$$

$$\frac{\partial T}{\partial t} + \mathbf{u} \cdot \nabla T = \nabla^2 T + Q \tag{3}$$

where $\mathbf{u}$ is the velocity, P is the pressure, η is the viscosity (temperature-dependent Newtonian), T is the temperature, $\mathbf{e}_r$ is the unit vector in the radial direction, and Q is an internal heat source (and/or sink). Ra is the Rayleigh number given by

$$Ra = \frac{\rho_m g \alpha \Delta T {R_p}^3}{\kappa \eta_0}, \tag{4}$$

where ρ_m is the average mantle density, g is the gravitational acceleration, α is the coefficient of thermal expansion, ΔT is the initial super-adiabatic temperature difference across the mantle, R_p is the planet's radius, κ is the thermal diffusivity, and η_0 is the mantle reference viscosity. Table 1 shows the values we use for these and other parameters. An important note here for comparing CitcomS results with other work is that the Rayleigh number is usually defined by a layer thickness, D, however CitcomS uses, R_p, the radius of the planet, for the length scale instead. For efficiency, CitcomS computations are parallelized (Tan et al., 2006). We model incompressible flow using the Boussinesq approximation.

We have made several changes and additions to the CitcomS code. The original code keeps mantle internal heating constant through time. However, because heat production results from the decay of radioisotopes, it is more realistic to have it decrease accordingly using the calculations described by Turcotte and Schubert (2014). Crustal enrichment of radioisotopes has also been added. We have incorporated the cooling of the planet's core, which is treated based on the coupled core and mantle thermal evolution model developed by Stevenson et al. (1983) As the core cools, the heat from the core heats the mantle from below, while the core-mantle boundary (CMB) temperature decreases.

2.2 Melt production

The largest modification to CitcomS is the incorporation of melting calculations. Much of the work on melting in Mars' mantle (Li & Kiefer, 2007; Kiefer, 2003; Kiefer & Li, 2016; Ruedas et al., 2013) was performed in 2D spherical axisymmetric geometry (or 2D Cartesian in the case of Tosi et al. (2013)) rather than 3D. With the exception of Ruedas et al. (2013), these also do not consider the decrease in radioisotope abundances through time or the thermodynamics of core cooling and solidification. Spherical 3D modeling incorporating decaying heating as well as crustal enrichment of radioisotopes has become more common over the past few years (Sekhar & King, 2014; Plesa et al., 2016, 2018). Because the melting formulation is new to CitcomS, we describe it in some detail below.

The first step in melt calculations is to calculate the equilibrium melt fraction, which for a given composition is a function of temperature and pressure. We calculate melt fraction (by mass) using the empirically derived parameterization of Katz et al. (2003) for dry peridotite melting at upper mantle pressures. We convert this mass fraction to a volume fraction given the solid mantle density (herein $3500\,\mathrm{kg\,m^{-3}}$) and the presumed melt density ($3000\,\mathrm{kg\,m^{-3}}$). The melt fraction algorithm of Katz et al. (2003) was developed by fitting experimental data on equilibrium melting of peridotite and is valid up to approximately 8 GPa. Katz et al. (2003) has since found broad application in geodynamic mantle convection codes such as CitcomS (e.g., Citron et al. (2018); Šrámek and Zhong (2012)), as well as ASPECT and adaptations thereof (e.g., Dannberg and Heister (2016)). While Katz et al. (2003) was originally published with terrestrial melting in mind, it has been applied to calculate melt productivity in convection models of the Martian mantle by Citron et al. (2018), Kiefer and Li (2016), and Šrámek and Zhong (2012). According to Šrámek and Zhong (2012) and Kiefer and Li (2016), the Katz et al. (2003) solidus is close to experimentally derived Mars solidi, such as those of Bertka and Holloway (1994); Agee and Draper (2004); Matsukage et al. (2013), using inferred Martian mantle compositions. The utility of Katz et al. (2003) is that it includes a solidus, liquidus, and a relatively straightforward nonlinear way to calculate melt fraction. Earlier geodynamic modeling employed simpler methods, such as Kiefer (2003) linearly increasing melt fraction between the solidus and assuming the liquidus is a fixed temperature above the solidus. We use the liquidus and lherzolite liquidus of Katz et al. (2003) for dry peridotite. However, we replace their solidus with that of Duncan et al. (2018). The Katz et al. (2003) solidus in degrees Celsius as a function of pressure P in GPa, 1085.7 + 132.9 P - 5.1 P^2, is higher than the Mars solidus of Duncan et al. (2018), 1088 + 120.2 P − 4.877 P^2 by up to 45°C (at 4 GPa) in the range of depths in which our models produce melt (see Figure 2).

The melt fraction by mass obtained from this modified katz2003new method is then converted to a fraction by volume according to the equation

$$X_{vol} = \frac{\rho_s}{\rho_m \left(\frac{1}{X_{mass}} - 1\right) + \rho_s} \tag{5}$$

where X_{vol} is the melt fraction by volume, X_{mass} is the melt fraction by mass, ρ_s is the solid mantle density ($3500\,\mathrm{kg\,m^{-3}}$, and rho_m is the melt density ($3000\,\mathrm{kg\,m^{-3}}$). From this point on, the melt fraction X refers to the volume fraction.

Melt production computations must consider not only the portion of a region that is molten (melt fraction), but also the movement of the mantle material through the melting region. Based on equation B1 of Watson and McKenzie (1991), $\dot{M}$, the instantaneous amount (herein, volume) of melt per unit (volume) of mantle material produced per unit time, is the material derivative of the equilibrium melt fraction X (by volume),

$$\dot{M} = \frac{DX}{Dt} = \frac{\partial X}{\partial t} + \mathbf{u} \cdot \nabla X. \tag{6}$$

Using the chain rule, $\dot{M}$ can be written in terms of the partial derivatives of melt fraction with respect to temperature and pressure.

$$\dot{M} = \frac{DX}{Dt} = \frac{\partial X}{\partial T}\frac{DT}{Dt} + \frac{\partial X}{\partial P}\frac{DP}{DT} = \frac{\partial X}{\partial T}\left(\frac{\partial T}{\partial t} + \mathbf{u} \cdot \nabla T\right) + \frac{\partial X}{\partial P}\left(\frac{\partial P}{\partial t} + \mathbf{u} \cdot \nabla P\right) \tag{7}$$

Assuming $\partial P/\partial t$ is zero and pressure is hydrostatic, then

$$\dot{M} = \frac{\partial X}{\partial T}\left(\frac{\partial T}{\partial t} + \mathbf{u} \cdot \nabla T\right) - \frac{\partial X}{\partial P}\bar{\rho} g u_r \tag{8}$$

where u_r is the radial component of velocity, and $\bar{\rho}$ is the radial profile of density. The volume of melt produced is calculated by integrating $\dot{M}$ over the element volumes using Gaussian quadrature.

2.3 Model cases

2.3.1 Rheology

We start by modeling a structural reference case, with a uniform lithosphere thickness rather than a hemispheric dichotomy. We run 18 models with this "uniform" structure, testing three values each for the initial CMB temperature (1720 K, 1870 K, 2020 K) and crustal HPE enrichment factor (5x, 10x, 15x), and two values for the activation energy E* ($117\,\mathrm{kJ\,mol^{-1}}$, $350\,\mathrm{kJ\,mol^{-1}}$). The initial HPE concentrations are derived from the present-day bulk concentrations from Wänke and Dreibus (1994) (Table 1), projected back in time. Based on Christensen (1983), activation energy is divided by the stress exponent n to approximate a power law rheology for olivine. Typically n is taken to be 3, but we vary the effective activation energy, corresponding to testing values of n=3 (dislocation creep) and n=1 (diffusion creep). Thus to approximate n=3, the nominal activation energy of $350\,\mathrm{kJ\,mol^{-1}}$ becomes $117\,\mathrm{kJ\,mol^{-1}}$ (low activation energy cases), while for n=1, we keep the activation as $350\,\mathrm{kJ\,mol^{-1}}$ (high activation energy cases).

The temperature and pressure (depth) dependent viscosity η is given, in dimensional form, by

$$\eta = A \cdot \eta_0 \cdot \exp\left(\frac{E_a + PV_a}{RT} - \frac{E_a + PV_a}{R(\Delta T + T_s)}\right) \tag{9}$$

where η_0 is is the reference viscosity ($1.0 \times 10^{21}\,\mathrm{Pa\,s}$), E_a is the activation energy (either 117 or $350\,\mathrm{kJ\,mol^{-1}}$), P is the pressure, V_a is the activation volume ($6.6\,\mathrm{cm^3\,mol^{-1}}$), R is the ideal gas constant, and T is the absolute potential temperature. The pre-exponential factor A is to control the viscosity by layer. To enforce a strong (initially 100 km thick) lithosphere, from the surface to 100 km depth, A = 10. From 100 km to 1000 km depth, A = 0.1, establishing a weak asthenosphere. From 1000 km depth to the CMB, A = 10, accounting for a strong transition zone rheology.

2.3.2 Temperature initial condition

The initial mantle temperature profile is set to a uniform temperature T_m (here, ΔT = 1500K) everywhere with cold and hot thermal boundary layers are added at the top and bottom, respectively. Small magnitude (0.01 ΔT) spherical harmonic degree 8, order 6 perturbations are added at all layers to initiate convection. The boundary layer temperatures are calculated by adjusting T_m based on 1D conductive cooling (at the top) or heating (bottom) of a half-space after a "half-space age". The top boundary layer is thus achieved by adjusting the constant temperate profile according to:

$$T(r) = T_m - (T_m - T_{surf}) \cdot \text{erf}\left(\frac{R - r}{2\sqrt{(a)}}\right) \tag{10}$$

and similarly the bottom boundary layer is created by

$$T(r) = T_m + (T_{cmb} - T_m) \cdot \text{erf}\left(\frac{r - r_{cmb}}{2\sqrt{(a)}}\right) \tag{11}$$

where $T(r)$ is the initial temperature at radius r, T_{surf} is the surface temperature (220 K), T_{cmb} is the initial CMB temperature, R is the radius of the planet (3389.5 km), r_{cmb} is the radius of the CMB, and a is the conductive cooling/heating age of the half-space. For all 18 uniform structure cases, The initial error function temperature profile, with top and bottom boundary layers, is based on a half-space age of 100 Myr.

2.3.3 Geoid Comparison

We compare the power spectrum of each of the geoids output by our models to the power spectrum of the observed Martian geoid with the effect of Tharsis' low degree ($\ell \leq$ 6) topography removed, i.e. Mars without Tharsis (MWT), as determined by the spherical harmonic gravity coefficients of Zuber and Smith (1997). We calculate the normalized root mean square error (NRMSE) of the model geoid power spectrum from spherical hamronic degrees ℓ = 2–6, given by

$$NRMSE = \sqrt{\frac{\sum_{\ell=2}^{6} \left(P_{\text{MWT, }\ell} - P_{\text{model, }\ell}\right)^2}{\sum_{\ell=2}^{6} P_{\text{MWT, }\ell}{}^2}} \tag{12}$$

where ℓ is the spherical harmonic degree, $P_{\text{MWT, l}}$ is the power in degree ℓ of the MWT geoid, $P_{\text{model, l}}$ is the power in degree ℓ of the model geoid. (The mean squared error is normalized by the mean of the squared values for MWT, and the numbers of points n = 5, cancel.) In this formulation, a geoid identical to MWT would have an NRMSE of 0, and a geoid with zero power for ℓ = 2–6 would have an NRMSE of 1.

2.3.4 Dichotomy

We repeat the range of nine high activation energy cases (3 crustal enrichments, 3 initial CMB temperatures) for models with a degree-1 hemispheric dichotomy structure (boundary along the equator). As opposed to the uniform cases described above, these are the nine "dichotomy" cases. The initial error function temperature profile in the southern hemisphere for these dichotomy cases is based on a thermal half-space age of 500 Myr. The initial temperature profile in the northern hemisphere is based on a thermal age of 100 Myr, as would result from the dichotomy-forming impact resetting the temperature profile ∼400 Myr after Mars formed. The initial southern hemisphere lithosphere is correspondingly set 100 km thicker than the northern hemisphere lithosphere by setting the viscosity in the lid to the maximum allowed value (as applied when truncating very high viscosities), which for our models is $10^5\eta_0 = 1 \times 10^{26}$ Pa s.

3 Results

3.1 Overview

Of the three parameters we varied (activation energy, crustal HPE enrichment, and initial CMB temperature), the results are most sensitive to the activation energy, and generally least sensitive to the CMB temperature. Therefore, the plots in the figures are grouped first by activation energy, specifically by the value of the stress exponent n that the nominal activation energy (350 $\mathrm{kJ\,mol^{-1}}$) is divided by in order to vary the effective activation energy. Above the bottom thermal boundary layer, the mean mantle temperatures and mean radial temperature profiles (geotherms) are not strongly influenced by the initial CMB temperature. Higher activation energy and, to a lesser degree, lower crustal enrichment and the the thicker southern lithosphere of the dichotomy cases, lead to a overall hotter mantle. However, these higher activation energies, and thus higher temperatures in the lower to mid-mantle, are reached with a thicker upper thermal boundary layer. As a consequence of the higher average temperatures they produce, lower enrichment and higher activation energy lead to more melt being produced for longer, in many cases nearly to the present day. Melting occurs primarily in the middle of the heads of plumes or the linear upwellings like those in Figure 5 (d) and (e). No inner core forms in any of our models, consistent with the InSight results constraining at most a very small, or, more likely, no inner core (Stähler et al., 2021; Irving et al., 2023).

3.2 Mantle Temperature and Geotherms

Figure 3 (a–c) shows the mean potential temperature profiles, or geotherms, at the time corresponding to present day for all the models, in three separate plots grouped according to the rheology: uniform structure, low activation energy; uniform structure, high activation energy; and dichotomy, high activation energy. On each of these three plots, the 1605 ± 100 K mid-mantle temperature from Huang et al. (2022) is marked by the vertical magenta lines, with the minimum and maximum dashed. The range of geotherms from the models of Smrekar et al. (2019) is shaded, with the lighter shading being below the mean, and the darker shading above it. All of the low activation energy geotherms fall several hundred kelvins below both Huang et al. (2022) and Smrekar et al. (2019). The mid-mantle temperatures for all high activation energy cases, including those with the dichotomy, plot within the range of Huang et al. (2022). The 5x and 10x enrichment cases also fall within the range of Smrekar et al. (2019), as do the 15x cases at depths less than $\sim$750 km. Our geotherms, not unlike Huang et al. (2022), are generally on the cooler side of the range of Smrekar et al. (2019), although they have a somewhat different shape such that the for depths between $\sim$100 and $\sim$500 km, the high activation energy cases with 5x and 10x enrichment rise above the mean of Smrekar et al. (2019).

The time evolution of the mean mantle potential temperature is likewise plotted in Figure 3 (d–f). The cases with lower crustal enrichment, that is those which retain more of the HPE in the mantle, heat up over the first few hundred million years as a result of this radiogenic heat. With the low activation energy rheology, this effect is only notable with the 5x enrichment, and even then very subtle. For high activation energy, this occurs with similar subtlety in the 10x cases, albeit stretched out over a longer time so that the peak temperature is later. Whereas the temperature increase with 5x enrichment is more pronounced and the peak $\sim$200-300 Myr later, which would be near the beginning of the Hesperian. With adding the dichotomy, the timing of the peak temperature is later still at about 3200 Ma, well into what would be the Hesperian.

Across all of our 27 cases, the mean present-day surface heat flux only ranges from 12.3 $\mathrm{mW\,m^{-2}}$ (high activation energy, enrichment = 5x, initial T_{CMB} = 1720 K) to 14.1 $\mathrm{mW\,m^{-2}}$ (low activation energy, enrichment = 5x, initial T_{CMB} = 2020 K). Of note, these values are only about half of the heat fluxes modeled by Plesa et al. (2015) and Plesa et al. (2016). Our mean surface heat fluxes correlate positively with initial CMB temperature, and negatively with activation energy. For high activation energy, the fluxes also increase with crustal enrichment, but curiously for low activation energy, the minimum surface heat flux occurs with 10x enrichment across all three initial CMB temperatures.

3.3 Geoids

The power spectra (from spherical harmonic degree ℓ=2–20) of the present-day geoids output by our models are plotted in Figure 4, with MWT in blue on each subplot. The NRMSE values for all 27 model power spectra are tabulated in Table 2. In terms of matching the MWT geoid power spectrum from $\ell = 2$–6 (i.e., having a lower NRMSE), the uniform structure, low activation energy, 15x enrichment cases have a remarkably good fit. (Though, to reiterate, the geotherms of these models fall well outside our constraint.) Several of the uniform, high activation cases, which do meet our geotherm constraint, also have a geoid that deviates relatively little from MWT, including all of the 10x enrichment cases and the 5x enrichment case with the hottest (initially 2020 K) CMB. For the uniform structure, the low activation energy cases with 5x enrichment, and the coolest (1720 K initial CMB) 10x enrichment case, have the poorest fits (high NRMSE) with MWT. Whereas for the uniform, high activation energy cases, it is the three 15x enrichment cases, and the coolest (1720 K initial CMB) 5x enrichment case, that have the poorest fits with MWT. Thus, broadly speaking, for low activation energies, the geoids of the 15x enrichment cases are favored, while for higher activation energies (without the dichotomy), the 10x enrichment cases are generally favored.

Turning to the dichotomy models (high activation energy only), there is less of a pattern in how well the geoids fit MWT, other than that the 5x enrichment cases are almost as poor at matching MWT as the 5x enrichment low activation energy cases without the dichotomy. In contrast to those well-fitting uniform, low activation energy, 15x enrichment cases, the hottest (2020 K initial CMB) 15x enrichment dichotomy case has the second poorest fit with MWT of all 27 models. Among the dichotomy cases, the hottest (2020 K initial CMB) 10x enrichment case best matches MWT, although the intermediate temperature (1870 K initial CMB) 15x enrichment case is still a relatively good fit.

3.4 3D Mantle Structure Evolution

All of the models develop long-lived plumes or plume-like linear upwellings. The cases without the dichotomy, both for low and high activation energies, tend to first develop a convection pattern dominated by degree-2, with two large antipodal plumes, but connected by a less prominent linear upwelling (Figure 5 (a, b)). This pattern gradually evolves into a persistent pattern dominated by a single linear upwelling that curves around much of planet–in some cases encircling it as a sinuous ring (Figure 5 (d, e, g, h)). When the upwelling remains discontinuous, one or both ends of the linear upwelling are warmer, with a broader head, where there is greater melting (Figure 5 (d, g)). The dichotomy models behave very differently. Within a few hundred million years they develop a degree-1 structure comprising a single large plume centered on the pole of the northern hemisphere–the one with thinner lithosphere and the warmer (younger) half-space initial temperature profile. Unlike the initially imposed step in lithospheric thickness–which gradually smooths out–this degree-1 convection pattern persists through present-day; although the plume becomes less vigorous as it, like the mantle as a whole, cools. While Mars is sometimes thought of as a 'one plume planet', the single upwelling plume is often assumed to form beneath the southern highlands and migrate toward the equatorial region (Zhong, 2009; Sekhar & King, 2014).*other cites here.* There is no geologic evidence supporting a plume forming beneath the Northern highlands and migrating to the south.

3.5 Melting

The total amount of melt over time, represented as the fraction of the mantle's volume that is molten (e.g., 0.1 = 10% of the mantle is melt) plotted in Figure 6 (a-e). This bulk melt fraction generally follows the trend of the mean mantle temperature, peaking after a few hundred million years, and then declining over the rest of the model run. The low activation energy cases, and the high activation energy cases with 10-15x enrichment and a cooler CMB, do tend to have an additional, earlier peak within the first 100 Myr, in some cases at the initial time step. In the cases with 15x enrichment and the initial CMB temperature of 1720 K, there is only this one early peak, corresponding with the rising of plumes.

The melt fraction in all models peaks with the mantle being at least several percent melt, with the 5x enrichment cases reaching bulk melt fractions well over 10%. All melting in our models occurs within a relatively narrow range of pressures/depths (2.6-4 GPa / $\sim$200–300 km) in the upper mantle, and the local melt percentages here can reach in excess of 40-50% by volume. The bulk melt fraction steadily drops after the early peak so that by $\sim$2000 Ma in the low activation energy cases and by $\sim$500-1000 Ma in the high activation energy cases, there is no discernible melt on the linear scales of Figure 6 (a–c). But this is in part misleading; a small mount of melt remains, in many cases persisting up to or near the present day, and this is more visible when the bulk melt fraction is plotted on a logarithmic scale as in Figure 6 (d–f). The overall amount of melt produced is not significantly affected by adding the dichotomy to the high activation energy cases, though it is marginally reduced.

The cases with low activation energy show much less spread in their melt production over time than the high activation energy cases when varying the enrichment and initial CMB temperature. Put another way, models with high activation energy are more sensitive to changes in the other parameters we varied. The coldest (15x enrichment) high activation energy models produce less melt through time than even the coldest low activation energy models, while the hottest (5x enrichment) high activation energy cases produce more melt than all of the low activation energy models. Each 5x and 10x enrichment case produces a melt volume within or above the nominal volume of the Tharsis rise (lighter gray shading in Figure 6, as does the low activation energy 15x enrichment case with the hottest (initially 2020 K) CMB. Yet, only the single warmest case of all 27 cases–the high activation energy, uniform structure model with 5x enrichment and the hottest (initially 2020 K) CMB–produces enough melt for Tharsis when accounting for limited extraction of mantle melt to the surface (darker shading in Figure 6).

Even on the logarithmic scale, the time of last melting is not clear from Figure 6, because the latest bulk melt fraction is more than 10 orders of magnitude lower than the peak. The precise model time and corresponding age of last melt production for each model case is listed in Table 3. Many cases are still producing melt at the end of the run, at present-day, and in others melting has only cut off within the past few hundred million years. These tend to be the lower enrichment cases. In all of the uniform 15x enrichment cases, melting shuts off well over 1 Ga. Melt continues for longer in the dichotomy 15x enrichment cases, even up to present day in the case of the hottest (initially 2020 K) CMB. Still not clear from either Figure 6 or Table 3 is that several models, mostly 10x enrichment cases, see melt production stop and restart one or more times before finally ending, or reaching present-day with melt present. These last trickles of melting are very small and localized.

4 Discussion

4.1 Model Summary

Of the three parameters varied (activation energy, crustal HPE enrichment, and initial CMB temperature), the results are most sensitive to the activation energy. The results are least sensitive to the initial CMB temperature. Higher activation energies, and thus higher temperatures in the lower to mid-mantle, result in a cooler and thicker lid, but also an overall hotter mantle. Corresponding with the higher average temperatures, lower enrichment and higher activation energy lead to more melt being produced for longer. The cases with a hotter CMB, and a cooler mantle due to lower concentrations of HPEs (higher crustal enrichment) are more influenced by bottom heating. In these cases, more vigorous plumes that rise at the beginning of the model run contribute more directly to the melting.

The results summarized and color coded in Figure 7 show whether each of our 27 model cases fits our constraints for (1) geotherms consistent with InSight results, (2) recent production of melt, (3) sufficient melt to produce Tharsis, and (4) matching the MWT geoid. Blue indicates the constraint is met, and red that it is not. Purple indicates an intermediate result (geoids) or that the constraint is met with qualification. For the geotherms, blue models have a mid-mantle temperature that falls within the 1605±100 K range of Huang et al. (2022), and red models fall well outside this range. For melt at present-day, models where melt is present at 4500 Myr into the run (0 Ma) are blue, and those with no melt in the past 200 Ma are red. The last melt in purple models occurs between 200 Ma and present-day, which given the limited resolution and high uncertainty in these models, could still be consistent with geologically recent melt. For melt volume production, blue models produce at least $1{\times}10^9$ of melt–sufficient to produce the Tharsis rise with 10% extraction. Red models produce $< 1{\times}10^8$ of melt, which is the minimum needed for Tharsis with 100% extraction. Purple models produce a total melt volume between these values, sufficient for Tharsis if melt extraction is $> 10\%$. For the geoids, an NRMSE (Table 2) < 0.6 is blue; $0.6 \leq$ NRMSE < 0.8 is purple, and NRMSE ≥ 0.8 is red.

Figure 7 shows that overall, the model cases most consistent with our constraints for Mars are the high activation energy cases with 5-10x crustal HPE enrichment, and more so the uniform structure cases than the dichotomy cases. The very cold geotherms of all nine low activation energy cases lead us to reject that rheology in favor the high activation energy rheology. The few examples in which a low activation energy case fully satisfies our constraint in any one category (blue) diverge, in that only a couple of 5x enrichment cases have melt at present-day, while it is the three low activation energy, 15x enrichment cases that produce geoids consistent with MWT. Indeed two of those three geoids are the best fits of all 27 models.

4.2 Geoids

Our models can only address the mantle contribution to the geoid, while the actual Martian geoid is also determined in part by crustal thickness and possible density anomalies within the crust. It is generally considered that lower spherical harmonic degrees of the geoid are dominated by the mantle, while higher degrees are dominated by the crust. Yet, in the case of Mars, the thickened crust of Tharsis dominates the lowest degrees of the geoid. Using the geoid obtained from the MWT gravity coefficients of Zuber and Smith (1997) to remove Tharsis, up to and including ℓ=6, mitigates the crustal contribution issue, such that we consider the crustal contribution negligible through ℓ=6. Furthermore, for l¿∼12, the geoid should be almost entirely determined by the crust. At the intermediate degrees, the crustal and mantle components should both be significant, and ideally we could separate these two and compare out model geoids with just the mantle component. However, resolving the question of these crustal contributions to the geoid is beyond the scope of this work, and we focus on the fit of our models with MWT through ℓ=6.

A subset of our models–particularly those with a uniform structure, high activation energy, and 5–10x enrichment–which meet our geotherm and melting constraints also meet our MWT geoid constraint. All three low activtion energy, 15x enrichment cases meet the geoid constraint as well. Indeed, these three include the geoid power spectra with the two lowest NRMSE values of all out models. Still, these three models perform unacceptably in that they cool far too quickly to meet our geotherm or present melt constraints.

4.3 Melting and Thermal Evolution

Many of our models produce a small amount of melt up to or near present-day, with some cases having small amounts of melting stopping and restarting. This is consistent with small, localized pulses of volcanism on Mars within the past few million to ∼100 million years. It should be noted that our models have limited resolution, for example ∼25 km vertical resolution, and still lower in the lateral direction over most of the mantle, including the 200-300 km melting depths. Therefore, it is possible that were these same parameters and initial conditions run at a significantly higher resolution–which would take an infeasible amount of computing time and power–melting could continue for a little longer, and would not stop and restart.

Producing sufficient melt for Tharsis while also producing a geoid power spectrum that is consistent with present-day Mars without the volcanically constructed topography of Tharsis (i.e., MWT) is very difficult. It is even difficult just to produce enough melt to account for the enormous volume of Tharsis, while also considering that only a fraction of melt produced in the mantle erupts on the surface. As depicted in Figure 7, only our single hottest case (high activation energy, 5x enrichment, 2020 K initial CMB temperature) fully fulfills our constraint assuming 10% melt extraction–and then only barely. (This case, alone among all nine 5x enrichment cases, satisfies our geoid constraint.) Yet this singular case still does not produce this quantity of melt quickly enough to allow for emplacement of the Tharsis rise by the late Noachian. The majority of our cases–and every case with 5-10x enrichment–produce at least a Tharsis-equivalent melt volume within the mantle, but this could only account for Tharsis if the majority (60%) of that melt were extracted to the surface.

We find the present-day geotherms from our models with the high activation energy rheology to be very consistent with present day Mars, while the geotherms of the low activation energy are hundreds of degrees colder than inferred from the results of InSight and previous modeling. It is, however, remarkable that despite the cold mean geotherms, the 5x enrichment cases with this low activation energy rheology are able to locally produce small volumes of melt up to or near present-day. The large discrepancy in geotherms does lead us to broadly reject the low activation energy rheology, so much so that this was not considered when modeling the dichotomy.

With regard to crustal HPE enrichment, and rather unsurprisingly, Figure 7 also reflects how the melting results favor lower crustal enrichment, which is somewhat at odds with the body of work favoring 10-15x enrichment–as well as the the geoid power spectra of our models. Nevertheless, most of the 10x cases with high activation energy produce melt up to or near present-day, and up to about ℓ=6 the geoid is a good fit with MWT. The 10x enrichment cases do produce significantly less melt overall, and early on, compared to the 5x cases. But even the 5x enrichment cases cannot produce enough melt, at least not quickly enough, to account for Tharsis without extremely efficient melt extraction.

The present day geotherms from the low activation energy cases are hundreds of degrees too cold to be consistent with what has been inferred for Mars, therefore we generally prefer the models with the higher activation energy. Nevertheless, the models with low activation energy and 15x enrichment provide the best-fitting geoid to observations. The power spectra for the 10x and 15x enrichment, high activation energy cases do still match well with the MWT geoid up to ℓ=6–8. Only at higher degrees is there significantly less power in the geoid for these cases compared to MWT, and the low activation energy 15x enrichment cases.

We do not consider in our modeling initial conditions arising from a magma ocean overturn (Elkins-Tanton et al., 2003; Elkins-Tanton, 2005). One might speculate that this would stabilize the mantle with regard to convection for some period of time, allowing the mantle to heat up. The interaction of the two effects of (1) cooling the mantle due to the overturn, and (2) the subsequent heating of the mantle due to stabilizing the mantle against convection, make it difficult to predict the impact of this condition without further analysis. That is beyond the scope of this work.

4.4 Effects of Adding the Dichotomy

Because of the large mismatch in geotherms with the low activation energy cases, and the associated difficulty in generating sufficient melt, we only ran the dichotomy cases with high activation energy. To first order, the geotherms of the dichotomy cases are very close to those of the corresponding cases without the dichotomy. In the long term, the mantle temperature is much more sensitive to crustal enrichment than it is to the initially thicker southern lithosphere and warmer northern hemisphere mantle. Recall that the initial temperature profile is also different with the dichotomy cases. The start time is taken to be 4100 Ma instead of 4500 Ma as in the uniform cases. To account for this, we initialize the southern hemisphere with an error function temperature profile corresponding to an age of 400 Ma (versus 100 Ma for the uniform case). The northern hemisphere initial condition is kept as a profile corresponding to an age of 100 Ma, consistent with a younger lithosphere and a large injection of heat from the putative large impactor responsible for the dichotomy (Marinova et al. (2008); Kiefer (2008); Andrews-Hanna et al. (2008)). The geoid power spectra produced by the dichotomy cases are often a poorer match to MWT than the corresponding uniform, high activation energy cases. The exceptions to this trend, in which the dichotomy improves the geoid fit, are either relatively minor (10x enrichment, 2020 K initial CMB) or among the 15x enrichment cases that we reject for not meeting other constraints. Including the hemispheric dichotomy also marginally decreases the cumulative melt production. However, the initially thicker southern lithosphere does make it easier to maintain a small amount of melt close to present-day, and this is not wholly attributable to the later start time with the same initial temperature profile in the northern hemisphere. That said, at best, adding the hemispheric dichotomy does not significantly improve the overall fitting of our constraints. We therefore still prefer the uniform cases.

5 Conclusions

Overall, we find that our results from the model cases with a high activation energy rheology, uniform structure (i.e., without the dichotomy), and 5–10x crustal HPE enrichment are the most consistent with the data we have for Mars from InSight and earlier missions. To a lesser degree, our results also favor the cases among these six with initial CMB temperature of 1870-2020 K (i.e., greater than the initial mid-mantle temperature), in that those are the cases without any red in Figure 7. That said, model results are least sensitive to the initial CMB temperature, as compared to the activation energy and crustal enrichment. This is good, in that the early CMB temperature is one of the most difficult parameters to constrain. Several of the dichotomy cases are almost as consistent with our constraints (i.e., blue or purple across Figure 7) and even maintain melt a little longer than the corresponding uniform cases. But both the geoid fit to MWT and the cumulative melt production for the 5–10x enrichment are made worse by adding the dichotomy. Therefore, we don't consider the dichotomy, at least as we model it, to be necessary or overall useful in fitting our constraints for Mars.

The present-day geotherms from our model cases with the high activation energy are all consistent with Huang et al. (2022) in supporting a present-day mantle cooler than most pre-mission estimates by Smrekar et al. (2019), and the 10x enrichment geotherms align with the middle of the 1605±100 K range. Among our preferred cases, cumulative and present-day melt production slightly favor the 5x enrichment cases over the 10x cases. But even with 10x enrichment, the Martian mantle is still capable of producing small amounts of melt near or at present-day, and neither the 5x nor 10x enrichment cases produce sufficient melt for Tharsis quickly enough without assuming a majority of mantle melt is extracted. A 10x crustal enrichment factor would be consistent with the modeling and seismic analysis of Drilleau et al. (2022), the geodynamic modeling of Samuel et al. (2021), and the lower end of the range inferred by Huang et al. (2022). A 10x enrichment factor also agrees well with the orbital gamma ray spectrometry data that indicate ∼50% of Mars' HPE are contained within its crust (Boynton et al., 2007; McLennan, 2001; Taylor et al., 2006). Furthermore, the geoid power spectra for $\ell = 2$–6, for all three uniform, high activation energy, 10x enrichment cases are in good agreement with the MWT geoid derived from Zuber and Smith (1997). Modifying the radial viscosity structure of these 5–10x enrichment models may further improve the poorer fit at higher degrees up to $\ell \approx 12$, above which crustal structure, rather than the mantle we model, should overwhelmingly dominate the geoid.

It is challenging to reconcile such a cool mantle at present with the amount of melting required throughout–and particularly early on in Martian history. It is nevertheless reassuring that our models, and thus a mantle as cool as Huang et al. (2022) find for present-day Mars, are still capable of producing small, localized amounts of melt, as the evidence of recent volcanism (Neukum et al., 2004; Susko et al., 2017; Horvath et al., 2021; Berman & Hartmann, 2002; Vaucher et al., 2009; Jaeger et al., 2010) necessitates, and the ongoing tectonic activity in Elysium observed by InSight (Stähler et al., 2022; Perrin et al., 2022; Broquet & Andrews-Hanna, 2022; Kiefer et al., 2023) suggests. Melt production is very sensitive to the mantle temperature, or more precisely the portion of the mantle that is above the solidus. Therefore more melt in the late pre-Noachian to early Hesperian, as is necessary to produce the Tharsis and Elysium rises, requires a hotter mantle and/or a lower solidus. A hotter mantle would have to cool more quickly in order to still reach the cool observed geotherms. The faster cooling of a hotter mantle may be facilitated by the consequently more vigorous convection, and considering the effect of compressible convection and, in particular, the latent heat of melting. Alternatively, or in addition to this, including the effect of water or CO_2 could depress the solidus enough to significantly increase melt production at a given temperature.

Data/Software Availability Statement

[For the purposes of peer review, our modified CitcomS code, the model output used to create the figures in this manuscript, and a README describing the contents are temporarily available via the following private Figshare link: `https://figshare.com/s/f667c63d0392cc47367b`. Note that this is a nearly 1 GB .zip file.] We use our own custom modifications to the geodynamic code CitcomS version 3.3.1 (Zhong et al., 2000; Tan et al., 2006; Zhong et al., 2008), the official code of which is available from Computational Infrastructure for Geodynamics (CIG) at `http://geoweb.cse.ucdavis.edu/cig/software/citcoms/`, as well as `https://doi.org/10.5281/zenodo.7271920`, or on GitHub at `https://github.com/geodynamics/citcoms`. Our modified CitcomS code, input (.cfg) files, and output files at 500 million year intervals will be made available at `https://data.lib.vt`

`.edu/`. Line plots were made with Matplotlib version 3.5.1 (Hunter, 2007), available under the Matplotlib license at `https://matplotlib.org/` or at `https://doi.org/10.5281/zenodo.5773480` . 3D plots were made with Paraview version 5.9.0 (Ahrens et al., 2005), available from `https://www.paraview.org/`. For working with the geoid output and data, we use pyshtools (Wieczorek & Meschede, 2018), with documentation and installation instructions available at `https://shtools.github.io/SHTOOLS/`.

Acknowledgments

This paper is InSight Contribution Number 333. S.D.K. And J.P.M. were funded by NASA InSight Participating Scientist Program grant #80NSSC18K1623.

References

Agee, C. B., & Draper, D. S. (2004). Experimental constraints on the origin of Martian meteorites and the composition of the Martian mantle. *Earth and Planet. Sci. Lett.*, *224*, 415–429. doi: https://doi.org/10.1016/j.epsl.2004.05.022

Aharonson, O., Zuber, M., & Rothman, D. (2001). Statistics of Mars' topography from the Mars Orbiter Laser Altimeter: Slopes, correlations, and physical models. *J. Geophys. Res.*, *106*, 23723-23735. doi: https://doi.org/10.1029/2000JE001403

Ahrens, J., Geveci, B., & Law, C. (2005). ParaView: An end-user tool for large data visualization. In *Visualization handbook.* Elesvier. (ISBN 978-0123875822)

Andrews-Hanna, J., Zuber, M., & Banerdt, W. (2008). The Borealis basin and the origin of the martian crustal dichotomy. *Nature Lett.*, *453*(26), 1212-1215. doi: https://doi.org/10.1038/nature07011

Banerdt, W. B., Smrekar, S. E., Banfield, D., Giardini, D., Golombek, M., Johnson, C. L., ... others (2020). Initial results from the InSight mission on Mars. *Nature Geosciences*, *13*, 183-189. doi: https://doi.org/10.1038/s41561-020-0544-y

Berman, D. C., & Hartmann, W. K. (2002). Recent fluvial, volcanic, and tectonic activity on the Cerberus plains of Mars. *Icarus*, *159*(1), 1–17. doi: https://doi.org/10.1006/icar.2002.6920

Bertka, C. M., & Holloway, J. R. (1994). Anhydrous partial melting of an iron-rich mantle I: subsolidus phase assemblages and partial melting phase relations at 10 to 30 kbar. *Contributions to Mineralogy and Petrology*, *115*, 313–322. doi: https://doi.org/10.1007/BF00310770

Boynton, W. V., Taylor, G. J., Evans, L. G., Reedy, R. C., Starr, R., Janes, D. M., ... Hamara, D. K. (2007). Concentration of h, si, cl, k, fe, and th in the low- and mid-latitude regions of mars. *Journal of Geophysical Research*, *112*(E12). doi: https://doi.org/10.1029/2007je002887

Broquet, A., & Andrews-Hanna, J. C. (2022). Geophysical evidence for an active mantle plume underneath Elysium Planitia on Mars. *Nature Astronomy*, 1–10. doi: https://doi.org/10.1038/s41550-022-01836-3

Carr, M. H. (1973). Volcanism on Mars. *J. Geophys. Res.*, *78*, 4049-4062. doi: https://doi.org/10.1029/JB078i020p04049

Christensen, U. (1983). Convection in a variable-viscosity fluid: Newtonian versus power-law rheology. *Earth and Planet. Sci. Lett.*, *64*, 153–162. doi: https://doi.org/10.1016/0012-821X(83)90060-2

Citron, R. I., Manga, M., & Tan, E. (2018). A hybrid origin of the Martian crustal dichotomy: Degree-1 convection antipodal to a giant impact. *Earth and Planet. Sci. Lett.*, *491*, 58-66. doi: https://doi.org/10.1016/j.epsl.2018.03.031

Dannberg, J., & Heister, T. (2016). Compressible magma/mantle dynamics: 3-D, adaptive simulations in ASPECT. *Geophysical Journal International*, *207*(3), 1343–1366. doi: https://doi.org/10.1093/gji/ggw329

Drilleau, M., Samuel, H., Garcia, R. F., Rivoldini, A., Perrin, C., Michaut, C., … Banerdt, W. B. (2022). Marsquake locations and 1-d seismic models for mars from InSight data. *Journal of Geophysical Research: Planets*, *127*(9). doi: https://doi.org/10.1029/2021je007067

Duncan, M. S., Schmerr, N. C., Bertka, C. M., & Fei, Y. (2018). Extending the solidus for a model iron-rich Martian mantle composition to 25 GPa. *Geophysical Research Letters*, *45*(19), 10,211-10,220. doi: https://doi.org/10.1029/2018GL078182

Elkins-Tanton, L. T. (2005). Possible formation of ancient crust on mars through magma ocean processes. *Journal of Geophysical Research*, *110*(E12). doi: https://doi.org/10.1029/2005je002480

Elkins-Tanton, L. T., Parmentier, E. M., & Hess, P. C. (2003). Magma ocean fractional crystallization and cumulate overturn in terrestrial planets: Implications for Mars. *Meteoritics & Planetary Science*, *38*(12), 1753–1771. doi: https://doi.org/10.1111/j.1945-5100.2003.tb00013.x

Giardini, D., Lognonné, P., Banerdt, W. B., Pike, W. T., Christensen, U., Ceylan, S., … others (2020). The seismicity of Mars. *Nature Geoscience*, *13*(3), 205–212. doi: https://doi.org/10.1038/s41561-020-0539-8

Hager, B. H., Clayton, R. W., Richards, M. A., Comer, R. P., & Dziewoński, A. M. (1985). Lower mantle heterogeneity, dynamic topography and the geoid. *Nature*, *313*, 541–545.

Harder, H. (1998, July). Phase transitions and the three-dimensional planform of thermal convection in the Martian mantle. *Journal of Geophysical Research: Planets*, *103*(E7), 16775–16797. doi: https://doi.org/10.1029/98je01543

Harder, H. (2000). Mantle convection and the dynamic geoid of Mars. *Geophys. Res. Lett.*, *27*(3), 301-304. doi: https://doi.org/10.1029/2022JE007298

Harer, H., & Christensen, U. R. (1996). A one-plume model of Martian mantle convection. *Nature*, *380*, 507-509.

Hiesinger, H., & Head III, J. W. (2004). The Syrtis Major volcanic province, Mars: Synthesis from Mars global surveyor data. *Journal of Geophysical Research: Planets*, *109*(E1). doi: https://doi.org/10.1029/2003JE002143

Horvath, D. G., Moitra, P., Hamilton, C. W., Craddock, R. A., & Andrews-Hanna, J. C. (2021). Evidence for geologically recent explosive volcanism in Elysium Planitia, Mars. *Icarus*, *365*. doi: https://doi.org/10.1016/j.icarus.2021.114499

Huang, Q., Schmerr, N. C., King, S. D., Kim, D., Rivoldini, A., Plesa, A.-C., … others (2022). Seismic detection of a deep mantle discontinuity within Mars by InSight. *Proc. Natl. Acad. Sci. U.S.A.*, *119*(42). doi: https://doi.org/10.1073/pnas.2204474119

Hunter, J. D. (2007). Matplotlib: A 2d graphics environment. *Computing in Science & Engineering*, *9*(3), 90–95. doi: https://doi.org/10.1109/MCSE.2007.55

Irving, J. C. E., Lekić, V., Durán, C., Drilleau, M., Kim, D., Rivoldini, A., … Xu, Z. (2023). First observations of core-transiting seismic phases on Mars. *Proceedings of the National Academy of Sciences*, *120*(18). doi: https://doi.org/10.1073/pnas.2217090120

Jaeger, W. L., Keszthelyi, L. P., Skinner Jr., J. A., Milazzo, M. P., McEwen, A. S., Titus, T. N., … others (2010). Emplacement of the youngest flood lava on Mars: A short, turbulent story. *Icarus*, *205*(1), 230–243. doi: https://doi.org/10.1016/j.icarus.2009.09.011

Janle, P., & Erkul, E. (1990). Gravity studies of the Tharsis area on Mars. *Earth, Moon, Planets*, *53*, 217-232. doi: https://doi.org/10.1007/BF00055948

Katz, R. F., Spiegelman, M., & Langmuir, C. H. (2003). A new parameterization of hydrous mantle melting. *Geochemistry, Geophysics, Geosystems*, *4*(9). doi: https://doi.org/10.1029/2002GC000433

Khan, A., Ceylan, S., van Driel, M., Giardini, D., Lognonné, P., Samuel, H., … others (2021). Upper mantle structure of Mars from InSight seismic data. *Science*,

373(6553), 434–438. doi: https://doi.org/10.1126/science.abf2966
Kiefer, W. S. (2003). Melting in the martian mantle: Shergottite formation and implications for present-day mantle convection on Mars. *Meteorit. Planet. Sci.*, *39*(12), 1815-1832.
Kiefer, W. S. (2008). Forming the martian great divide. *Nature*, *453*, 1191-1192. doi: https://doi.org/10.1038/4531191a
Kiefer, W. S., & Li, Q. (2016). Water undersaturated mantle plume volcanism on present-day Mars. *Meteorit. Planet. Sci.*, *51*(11). doi: https://doi.org/10.1111/maps.12720
Kiefer, W. S., Weller, M. B., Duncan, M. S., & Filiberto, J. (2023, March). Mantle plume magmatism in Elysium Planitia as constrained by InSight seismic observations. In *Lunar and planetary science conference.* The Woodlands, TX, USA.
King, S., & Redmond, H. (2005, March). The crustal dichotomy and edge-driven convection: A mechanism for Tharsis Rise volcanism. In *Lunar and planetary science conference.* The Woodlands, TX, USA. Retrieved from `https://www.lpi.usra.edu/meetings/lpsc2005/pdf/1960.pdf`
King, S. D. (2008). Pattern of lobate scarps on Mercury's surface reproduced by a model of mantle convection. *Nature Geoscience*, *1*(4), 229–232. doi: https://doi.org/10.1038/ngeo152
Knapmeyer-Endrun, B., Panning, M. P., Bissig, F., Joshi, R., Khan, A., Kim, D., ... others (2021). Thickness and structure of the martian crust from insight seismic data. *Science*, *373*(6553), 438–443. doi: https://doi.org/10.1126/science.abf8966
Li, Q., & Kiefer, W. S. (2007). Mantle convection and magma production on present-day Mars: Effects of temperature-dependent rheology. *Geophys. Res. Lett.*, *34*(L16203). doi: https://doi.org/10.1029/2007GL030544
Malin, M. C. (1977). Comparison of volcanic features of Elysium (Mars) and Tibesti (Earth). *GSA Bulletin*, *88*(7), 908–919. doi: https://doi.org/10.1130/0016-7606(1977)88⟨908:COVFOE⟩2.0.CO;2
Marinova, M. M., Aharonson, O., & Asphaug, E. (2008). Mega-impact formation of the Mars hemispheric dichotomy. *Nature*, *119*, 1216-1219. doi: https://doi.org/10.1038/nature07070
Matsukage, K. N., Nagayo, Y., Whittaker, M. L., Takahashi, E., & Kawasaki, T. (2013). Melting of the Martian mantle from 1.0 to 4.5 GPa. *Journal of Mineralogical and Petrological Sciences*, *108*, 201–214. doi: https://doi.org/10.2465/jmps.120820
McLennan, S. M. (2001). Crustal heat production and the thermal evolution of mars. *Geophysical Research Letters*, *28*(21), 4019–4022. doi: https://doi.org/10.1029/2001gl013743
Mouginis-Mark, P., Zimbelman, J., Crown, D., Wilson, L., & Gregg, T. (2022). Martian volcanism: Current state of knowledge and known unknowns. *Geochemistry*, *82*. doi: https://doi.org/10.1016/j.chemer.2022.125886
Neukum, G., Jaumann, R., Hoffmann, H., Hauber, E., Head, J., A.T., B., ... the HRSC Investigator Team (2004). Recent and episodic volcanic and glacial activity on Mars revealed by the High Resolution Stereo Camera. *Nature*, *432*, 971-979. doi: https://doi.org/10.1038/nature03231
Neumann, G., Zuber, M., Wieczorek, M., McGovern, P., Lemoine, F., & Smith, D. (2004). Crustal structure of Mars from gravity and topography. *J. Geophys. Res.*, *109*(E08002). doi: https://doi.org/10.1029/2004JE002262
Perrin, C., Jacob, A., Lucas, A., Myhill, R., Hauber, E., Batov, A., ... Fuji, N. (2022). Geometry and Segmentation of Cerberus Fossae, Mars: Implications for Marsquake Properties. *Journal of Geophysical Research: Planets*, *127*(1). doi: https://doi.org/10.1029/2021je007118
Phillips, R., Zuber, M., Solomon, S., Golombek, M., Jakosky, B., Banerdt, W., ...

Hauck II, S. (2001). Ancient geodynamics and global-scale hydrology on Mars. *Science*, *291*, 2587-2591. doi: https://doi.org/10.1126/science.1058701

Platz, T., Michael, G. G., & Neukum, G. (2010). Confident thickness estimates for planetary surface deposits from concealed crater populations. *Earth and Planet. Sci. Lett.*, *293*, 388–395. doi: https://doi.org/10.1016/j.epsl.2010.03.012

Plesa, A.-C., Grott, M., Tosi, N., Breuer, D., Spohn, T., & Wieczorek, M. (2016). How large are present-day heat flux variations across the surface of Mars? *J. Gephys. Res. Planets*, *121*, 2386-2403. doi: https://doi:10.1002/2016JE005126

Plesa, A.-C., Knapmeyer, M., Golombek, M., Breuer, D., Grott, M., Kawamura, T., ... Weber, R. (2018). Present-day Mars' seismicity predicted From 3-D thermal evolution models of interior dynamics. *Geophys. Res. Lett.*, *45*, 2580-2589. doi: https://doi.org/10.1002/2017GL076124

Plesa, A.-C., Tosi, N., Grott, M., & Breuer, D. (2015). Thermal evolution and Urey ratio of Mars. *J. Gephys. Res. Planets*, *120*, 995-1010. doi: https://doi.org/10.1002/2014JE004748

Richardson, J., Wilson, J., Connor, C., Bleacher, J., & Kiyosugi, K. (2017). Recurrence rate and magma effusion rate for the latest volcanism on Arsia Mons, Mars. *Earth Planet. Sci. Lett.*, *458*, 170-178. doi: https://doi.org/10.1016/j.epsl.2016.10.040

Roberts, J. H., & Zhong, S. (2004). Plume-induced topography and geoid anomalies and their implications for the Tharsis rise on Mars. *J. Geophys. Res. Planets*, *109*(E03009). doi: https://doi.org/10.1029/2003JE002226

Roberts, J. H., & Zhong, S. (2006). Degree-1 convection in the Martian mantle and the origin of the hemispheric dichotomy. *J. Geophys. Res. Planets*, *111*(E06013). doi: https://doi.org/10.1029/2005JE002668

Ruedas, T., Tackley, P. J., & Solomon, S. C. (2013). Thermal and compositional evolution of the martian mantle: Effects of water. *Physics of the Earth and Planetary Interiors*, *220*, 50-72. doi: https://doi.org/10.1016/j.pepi.2013.04.006

Samuel, H., Ballmer, M. D., Padovan, S., Tosi, N., Rivoldini, A., & Plesa, A.-C. (2021). The thermo-chemical evolution of Mars with a strongly stratified mantle. *J. Geophys. Res. Planets*, *126*. doi: https://doi.org/10.1029/2020JE006613

Sekhar, P., & King, S. D. (2014). 3D spherical models of Martian mantle convection constrained by melting history. *Earth Planet. Sci. Lett.*, *388*, 27–37. doi: https://doi.org/10.1016/j.epsl.2013.11.047

Smrekar, S. E., Lognonné, P., Spohn, T., Banerdt, W. B., Breuer, D., et al. (2019). Pre-mission InSights on the Interior of Mars. *Space Science Reviews*, *215*(1), 1–72. doi: https://doi.org/10.1007/s11214-018-0563-9

Šrámek, O., & Zhong, S. (2012). Martian crustal dichotomy and Tharsis formation by partial melting coupled to early plume migration. *Journal of Geophysical Research: Planets*, *117*(E1). doi: https://doi.org/10.1029/2011JE003867

Stähler, S. C., Khan, A., Banerdt, W. B., Lognonné, P., Giardini, D., Ceylan, S., ... others (2021). Seismic detection of the martian core. *Science*, *373*(6553), 443–448. doi: https://doi.org/10.1126/science.abi7730

Stähler, S. C., Mittelholz, A., Perrin, C., Kawamura, T., Kim, D., Knapmeyer, M., ... others (2022). Tectonics of Cerberus Fossae unveiled by marsquakes. *Nature Astronomy*, *6*(12), 1376–1386. doi: https://doi.org/10.1038/s41550-022-01803-y

Stähler, S. C., Mittelholz, A., Perrin, C., Kawamura, T., Kim, D., Knapmeyer, M., ... Banerdt, W. B. (2022). Tectonics of Cerberus Fossae unveiled by marsquakes. *Nature Astronomy*, *6*(12), 1376–1386. doi: https://doi.org/10.1038/s41550-022-01803-y

Stevenson, D. J., Spohn, T., & Schubert, G. (1983). Magnetism and thermal evolution of the terrestrial planets. *Icarus*, *54*(3), 466–489. doi: https://doi.org/10.1016/0019-1035(83)90241-5

Susko, D., Karunatillake, S., Kodikara, G., Skok, J. R., Wray, J., Heldmann, J., ... Judice, T. (2017). A record of igneous evolution in Elysium, a major martian volcanic province. *Scientific Reports*, *7*(1). doi: https://doi.org/10.1038/srep43177

Tan, E., Choi, E., Thoutireddy, P., Gurnis, M., & Aivazis, M. (2006). GeoFramework: Coupling multiple models of mantle convection within a computational framework. *Geochem. Geophys. Geosyst.*, *7*(Q06001). doi: https://doi.org/10.1029/2005GC001155

Taylor, G. J., Boynton, W., Brückner, J., Wänke, H., Dreibus, G., Kerry, K., ... Drake, D. (2006). Bulk composition and early differentiation of mars. *Journal of Geophysical Research*, *112*(E3). doi: https://doi.org/10.1029/2005je002645

Tosi, N., Plesa, A.-C., & Breuer, D. (2013). Overturn and evolution of a crystallized magma ocean: A numerical parameter study for Mars. *J. Geophys. Res. Planets*, *118*, 1512-1528. doi: https://doi.org/10.1002/jgre.20109

Turcotte, D. L., & Schubert, G. (2014). *Geodynamics*. Cambridge, UK: Cambridge University Press. doi: https://doi.org/10.1017/CBO9780511843877

Šrámek, O., & Zhong, S. (2012). Martian crustal dichotomy and Tharsis formation by partial melting coupled to early plume migration. *J. Geophys. Res.*, *117*(E01005). doi: https://doi.org/10.1029/2011JE003867

van Thienen, P., Rivoldini, A., Van Hoolst, T., & Lognonné, P. (2006). A top-down origin for martian mantle plumes. *Icarus*. doi: https://doi:10.1016/j.icarus.2006.06.008.

Vaucher, J., Baratoux, D., Mangold, N., Pinet, P., Kurita, K., & Grégoire, M. (2009). The volcanic history of central Elysium Planitia: Implications for martian magmatism. *Icarus*, *204*(2), 418–442. doi: https://doi.org/10.1016/j.icarus.2009.06.032

Wänke, H., & Dreibus, G. (1994). Chemistry and accretion history of mars. *Philosophical Transactions of the Royal Society of London. Series A: Physical and Engineering Sciences*, *349*(1690), 285–293.

Watson, S., & McKenzie, D. (1991). Melt generation by plumes: a study of Hawaiian volcanism. *Journal of Petrology*, *32*(3), 501–537. doi: https://doi.org/10.1093/petrology/32.3.501

Watters, T., & Schubert, G. (2007). Hemispheres apart: The crustal dichotomy on Mars. *Annu. Rev. Earth Planet. Sci.*, *35*, 621-652. doi: https://doi:10.1146/annurev.earth.35.031306.140220

Wenzel, M. J., Manga, M., & Jellinek, A. M. (2004). Tharsis as a consequence of Mars' dichotomy and layered mantle. *Geophys. Res. Lett.*, *31*(L04702). doi: https://doi.org/10.1029/2003GL019306

Wieczorek, M. A., Broquet, A., McLennan, S. M., Rivoldini, A., Golombek, M., Antonangeli, D., ... others (2022). InSight constraints on the global character of the Martian crust. *J. Geophys. Res. Planets*, *127*. doi: https://doi.org/10.1029/2022JE007298

Wieczorek, M. A., & Meschede, M. (2018, August). SHTools: Tools for working with spherical harmonics. *Geochemistry, Geophysics, Geosystems*, *19*(8), 2574–2592. doi: https://doi.org/10.1029/2018gc007529

Zhong, S. (2009). Migration of Tharsis volcanism on Mars caused by differential rotation of the lithosphere. *Nature Geoscience*, *2*, 19-23. doi: https://doi.org/10.1038/NGEO392

Zhong, S., McNamara, A., Tan, E., Moresi, L., & Gurnis, M. (2008). A benchmark study on mantle convection in a 3-D spherical shell using CitcomS. *Geochem. Geophys. Geosyst.*, *9*(10). doi: https://doi.org/10.1029/2008GC002048

Zhong, S., Zuber, M. T., Moresi, L., & Gurnis, M. (2000). Role of temperature-dependent viscosity and surface plates in spherical shell models of mantle convection. *J. Geophys. Res.*, *105*(B5), 11,063-11,082. doi: https://doi.org/10.1111/maps.12720

Zuber, M., & Smith, D. (1997). Mars without Tharsis. *J. Geophys. Res.*, *102*(E12), 28,673-28,685. doi: https://doi.org/10.1029/97JE02527

Zuber, M., Solomon, S., Phillips, R., Smith, D., Tyler, G., Aharonson, O., ... Zhong, S. (2000). Internal structure and early thermal evolution of Mars from Mars Global Surveyor topography and gravity. *Science*, *287*(1788). doi: https://doi.org/10.1126/science.287.5459.1788

Tables

Table 1: Summary of parameters and initial conditions used in our models.

Parameter	Value
Mean radius	3.3895×10^{6} m
Core radius	1.830×10^{6} m
Mean mantle density	$3500\,\mathrm{kg\,m^{-3}}$
Gravitational acceleration (g)	$3.72\,\mathrm{m\,s^{-2}}$
Reference viscosity (η_0)	1.0×10^{21} Pa s
Activation energy (E*)	$117\,\mathrm{kJ\,mol^{-1}}$ (low)
	$350\,\mathrm{kJ\,mol^{-1}}$ (high)
Activation volume (V*)	$6.6\,\mathrm{cm^3\,mol^{-1}}$
Rayleigh number (Ra), mantle thickness[a]	1.4296×10^{7}
Thermal expansivity (α)	$2 \times 10^{-5}\,\mathrm{K^{-1}}$
Thermal diffusivity (κ)	$1 \times 10^{-6}\,\mathrm{m^2\,s^{-1}}$
Specific heat capacity (c_P)	$1.25 \times 10^{3}\,\mathrm{J\,kg^{-1}\,K^{-1}}$
Mantle adiabat	$0.15\,\mathrm{K\,km^{-1}}$
Surface Temperature (T_s)	220 K
Temperature difference (ΔT)	1500 K
Initial mantle temperature[b]	1720 K
Initial CMB temperature[b]	1720 K (1.0 ΔT)
	1870 K (1.1 ΔT)
	2020 K (1.2 ΔT)
Crustal HPE enrichment factor	5x
	10x
	15x
Present-day bulk ^{238}U	15.88 ppm [c]
Present-day bulk ^{235}U	0.11 ppm [c]
Present-day bulk ^{232}Th	56.0 ppm [c]
Present-day bulk K	305 ppm [c]
Present-day bulk ^{40}K	36.3 ppm [c]

[a] Rescaled from model because CitcomS uses radius instead of mantle thickness for its Ra
[b] Potential temperature: excludes adiabat
[c] Present-day bulk silicate Mars HPE concentrations from Wänke and Dreibus (1994)

Table 2: Quantitative comparison of our model geoids (model) to that of Mars without Tharsis (MWT) (Zuber & Smith, 1997) for degrees ℓ=2–6.

Rheology	Enrichment	T_{CMB}	NRMSE[a]
Uniform, low E*	5x	1720 K	0.9877
Uniform, low E*	5x	1870 K	0.9693
Uniform, low E*	5x	2020 K	0.9601
Uniform, low E*	10x	1720 K	0.8245
Uniform, low E*	10x	1870 K	0.7820
Uniform, low E*	10x	2020 K	0.7619
Uniform, low E*	15x	1720 K	0.3918
Uniform, low E*	15x	1870 K	0.2046
Uniform, low E*	15x	2020 K	0.5368
Uniform, high E*	5x	1720 K	0.8826
Uniform, high E*	5x	1870 K	0.7702
Uniform, high E*	5x	2020 K	0.4637
Uniform, high E*	10x	1720 K	0.4260
Uniform, high E*	10x	1870 K	0.5013
Uniform, high E*	10x	2020 K	0.4892
Uniform, high E*	15x	1720 K	2.185
Uniform, high E*	15x	1870 K	1.635
Uniform, high E*	15x	2020 K	1.128
Dichotomy, high E*	5x	1720 K	0.9459
Dichotomy, high E*	5x	1870 K	0.8921
Dichotomy, high E*	5x	2020 K	0.7433
Dichotomy, high E*	10x	1720 K	0.8787
Dichotomy, high E*	10x	1870 K	0.8516
Dichotomy, high E*	10x	2020 K	0.3955
Dichotomy, high E*	15x	1720 K	0.7161
Dichotomy, high E*	15x	1870 K	0.5515
Dichotomy, high E*	15x	2020 K	1.978

[a] See text.

Table 3: Model time and age of last melt production

Rheology[a]	Enrichment	T_{CMB}	Model time	Age BP[b,c]
Uniform, low E*	5x	1720 K	4500 Myr	0 Ma
Uniform, low E*	5x	1870 K	4483 Myr	17 Ma
Uniform, low E*	5x	2020 K	4500 Myr	0 Ma
Uniform, low E*	10x	1720 K	3154 Myr	1346 Ma
Uniform, low E*	10x	1870 K	3615 Myr	884 Ma
Uniform, low E*	10x	2020 K	4142 Myr	358 Ma
Uniform, low E*	15x	1720 K	2105 Myr	2395 Ma
Uniform, low E*	15x	1870 K	3129 Myr	1371 Ma
Uniform, low E*	15x	2020 K	2560 Myr	1940 Ma
Uniform, high E*	5x	1720 K	4500 Myr	0 Ma
Uniform, high E*	5x	1870 K	4500 Myr	0 Ma
Uniform, high E*	5x	2020 K	4500 Myr	0 Ma
Uniform, high E*	10x	1720 K	3756 Myr	744 Ma
Uniform, high E*	10x	1870 K	4500 Myr	0 Ma
Uniform, high E*	10x	2020 K	4354 Myr	146 Ma
Uniform, high E*	15x	1720 K	2080 Myr	2420 Ma
Uniform, high E*	15x	1870 K	3785 Myr	715 Ma
Uniform, high E*	15x	2020 K	4229 Myr	271 Ma
Dichotomy, high E*	5x	1720 K	4100 Myr	0 Ma
Dichotomy, high E*	5x	1870 K	4100 Myr	0 Ma
Dichotomy, high E*	5x	2020 K	4100 Myr	0 Ma
Dichotomy, high E*	10x	1720 K	4100 Myr	0 Ma
Dichotomy, high E*	10x	1870 K	4100 Myr	0 Ma
Dichotomy, high E*	10x	2020 K	4100 Myr	0 Ma
Dichotomy, high E*	15x	1720 K	3028 Myr	1072 Ma
Dichotomy, high E*	15x	1870 K	3210 Myr	890 Ma
Dichotomy, high E*	15x	2020 K	4100 Myr	0 Ma

[a] E* is activation energy.
[b] Uniform cases are taken to start at 4.5 Ga.
[c] Dichotomy cases are taken start 400 Myr later, at 4.1 Ga.

967 ## Figures

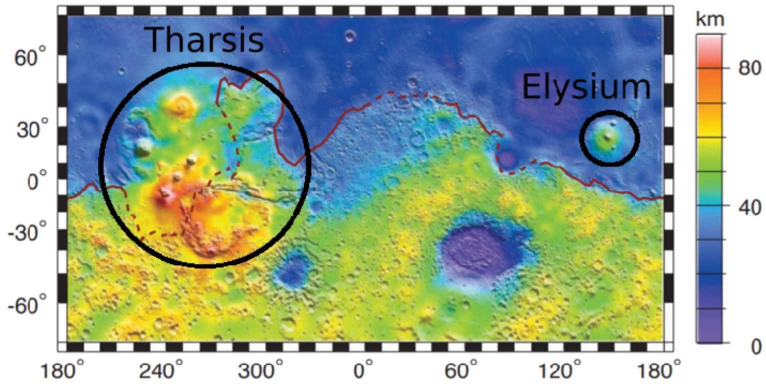

Figure 1: Crustal thickness map adapted from Zuber et al. (2000). The locations and approximate extent of Tharsis and Elysium are marked. The red line marks the dichotomy boundary. The line is dashed where the boundary is uncertain, in particular beneath Tharsis.

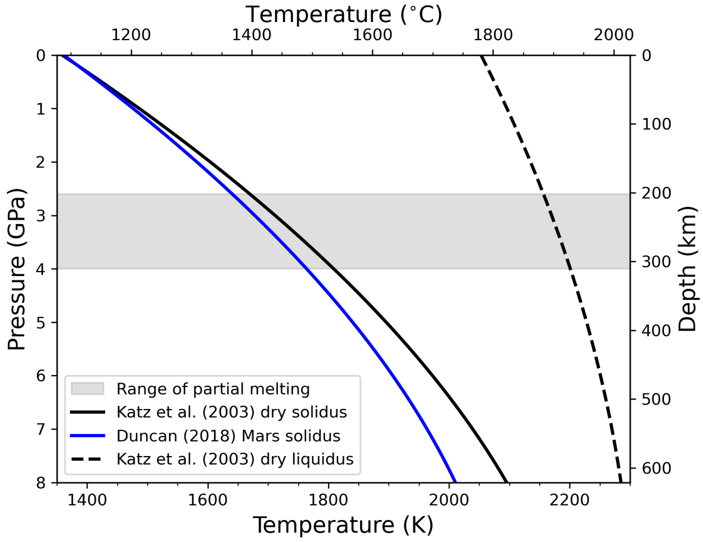

Figure 2: Comparison of the Katz et al. (2003) solidus for dry peridotite with the Mars solidus of Duncan et al. (2018) over the applicable depth range of Katz et al. (2003). The liquidus of Katz et al. (2003) is also plotted. Melting in our models is confined to a narrow range of pressures between 2.6 and 4 GPa, or approximately 200–300 km depth.

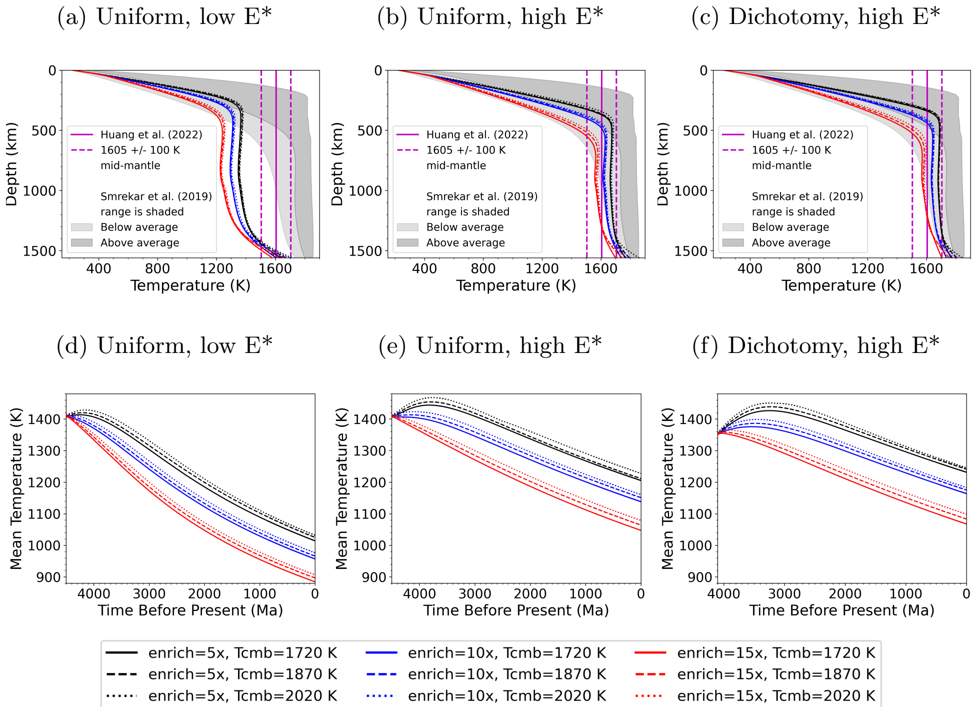

Figure 3: (a–c): Present-day geotherms, including the InSight derived mid-mantle temperature estimate of 1605±100 K by Huang et al. (2022) (vertical magenta lines), as well as the range of possible geotherms from Smrekar et al. (2019) (shaded). (d–e): Mean mantle temperature vs. time. E* is activation energy.

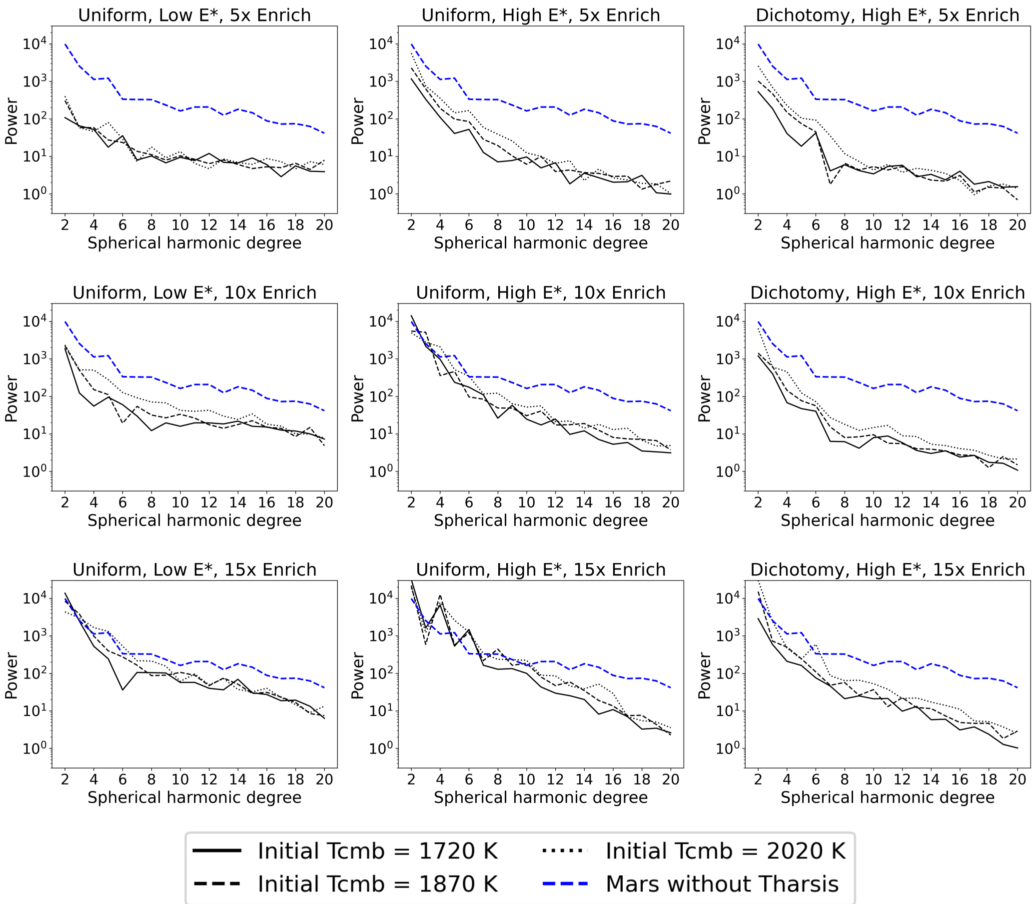

Figure 4: Power spectra (degrees ℓ=2–20) of our modeled present-day geoids (black) compared to the Mars without Tharsis (blue dashed) geoid derived from the gravity coefficients of Zuber and Smith (1997).

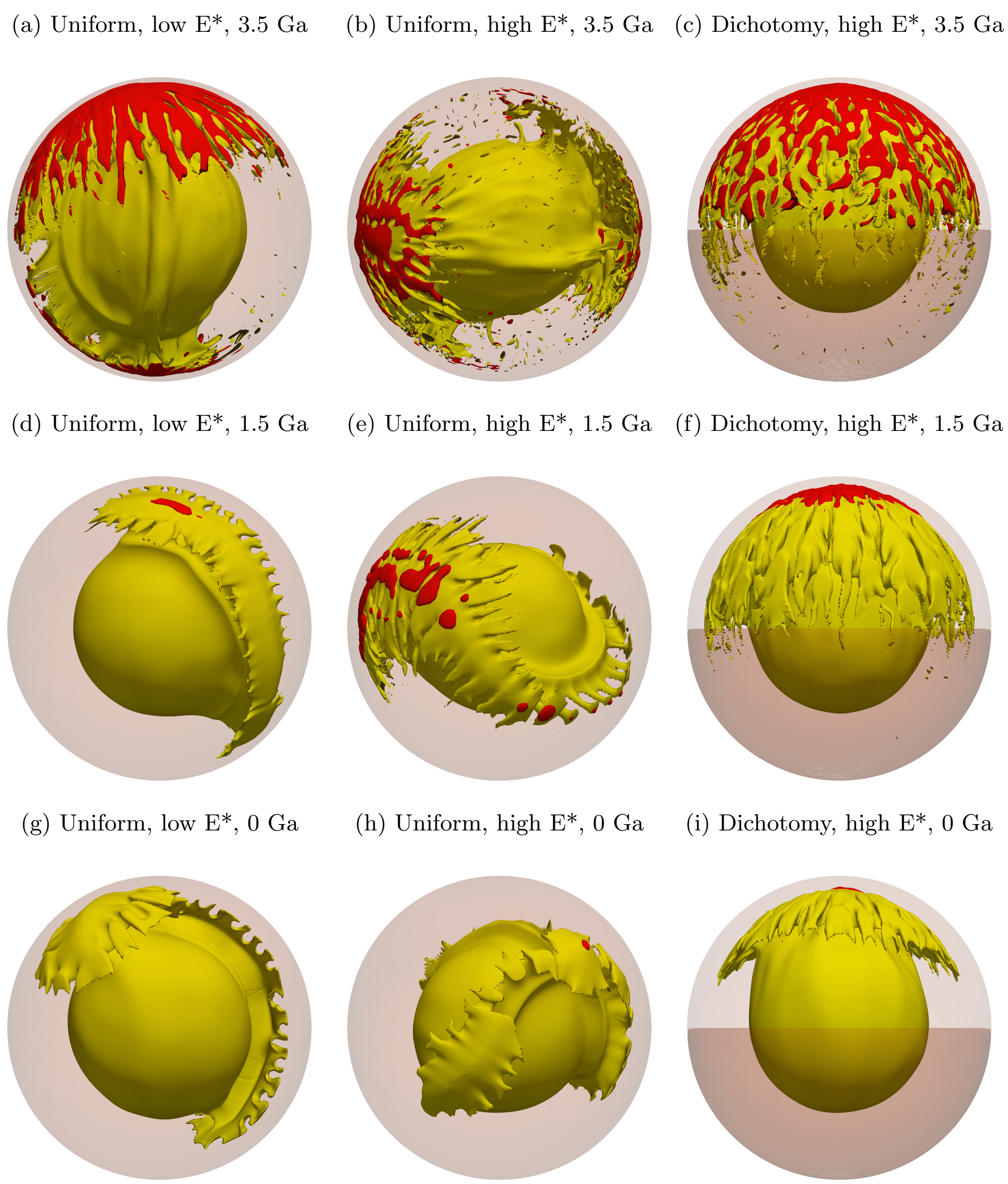

Figure 5: 3D plots of selected model cases with potential temperature isotherms (yellow) and melt (red) for all three (uniform, low activation energy; uniform, high activation energy; dichotomy, high activation energy) cases with 10x enrichment and initial T_{CMB} of 1870 K. The temperature and melt abundance vary widely both between the model cases and through time. Therefore, the plotted isotherms and melt thresholds for each model and time step are selected to be representative of the thermal structure and the highest melt concentration in the specified model at the specified time. The values chosen are as follows: (a) T = 1650 K, melt fraction $\geq$ 10%; (b) T = 1770 K, melt fraction $\geq$ 25%; (c) T = 1755 K, melt fraction $\geq$ 25%; (d) T = 1500 K, melt fraction $\geq$ 0.01%; (e) T = 1710 K, melt fraction $\geq$ 0.1%; (f) T = 1710 K, melt fraction $\geq$ 1%; (g) T = 1380 K, no melt present; (h) T = 1680 K, melt fraction $\geq$ 0.01%; and (i) T = 1680 K, melt fraction $\geq$ 1%. The southern hemisphere, with the initially thicker lithosphere, is darker in all dichotomy plots (c, f, i). For the remaining plots, north is approximately up, but some rotation has been done to better show the structure and melt.

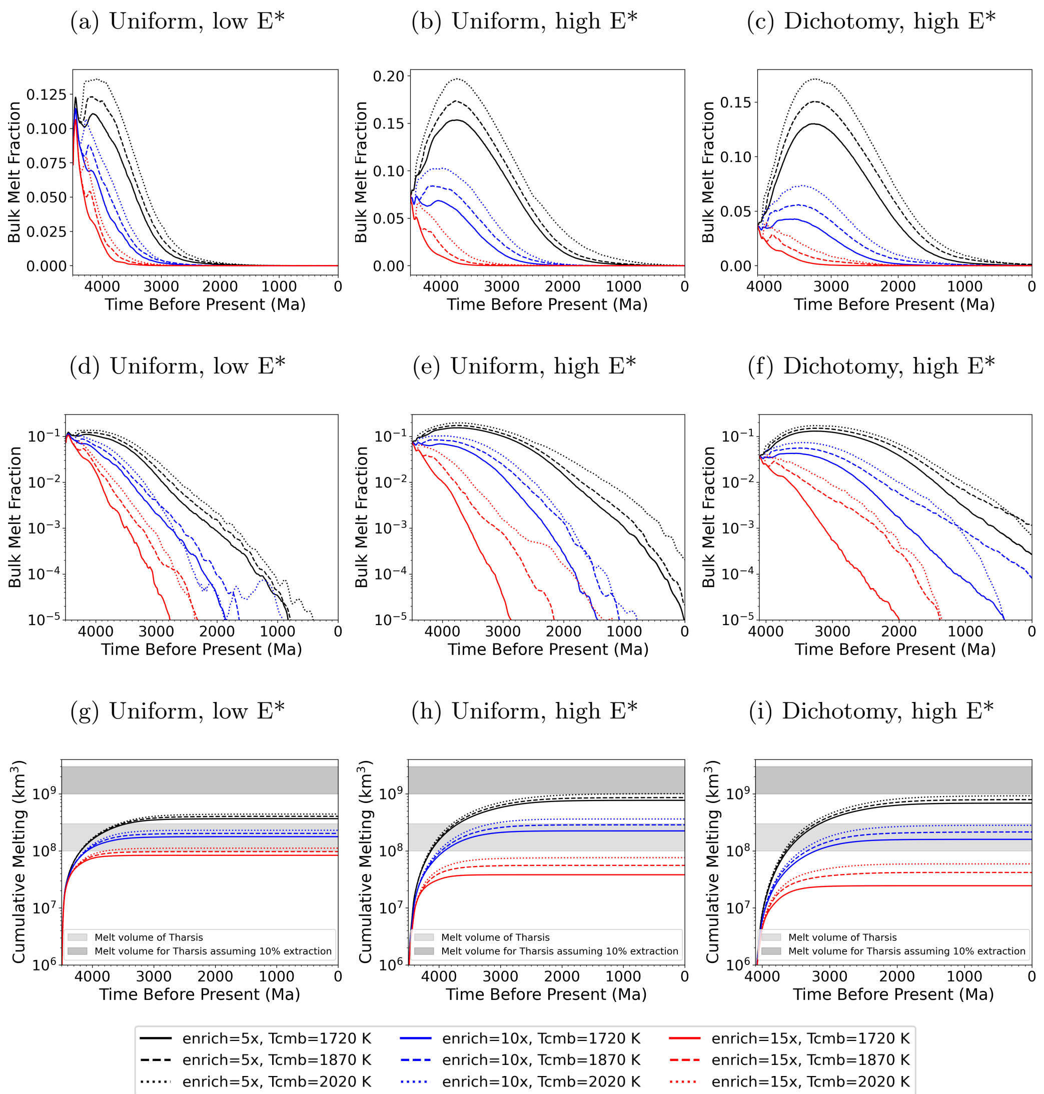

Figure 6: Melt and melt production over time. The bulk melt fraction is the fraction of the total mantle (out of 1.0) that is molten at a given time. This is shown here both on a linear and logarithmic scale. Cumulative melt is the integral of the mantle melt production rate over time. On the cumulative melt plots (g–i), the approximate amount of melt (1–3 $\times 10^8$ km^3) required to produce Tharsis is shaded in lighter gray. However, only a fraction of the melt (here assumed to be 10%) produced in the mantle is extracted to and erupted on the surface. The darker gray shading on these same plots is the required melt volume multiplied by ten (1–3 $\times 10^9$ km^3) to account for this.

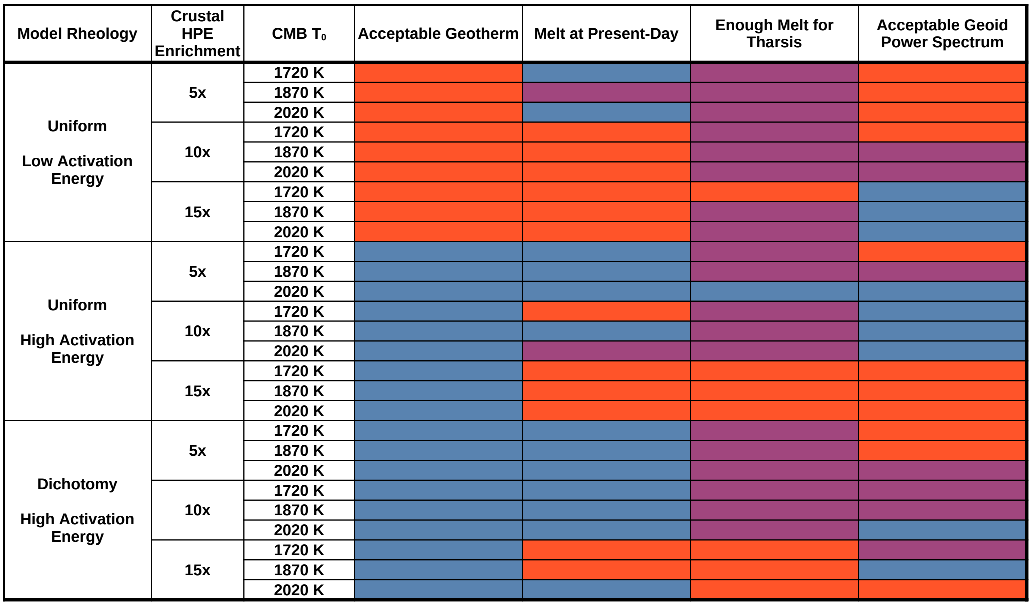

Figure 7: Blue indicates the constraint is met, and red that it is not. Purple indicates an intermediate result (geoids) or that the constraint is met with qualification. See discussion text for the quantitative meaning of these colors for each column.